Chapter 7

DISCUSSION

7.1 Nature of the ULXs

In the previous chapter, we confirmed that the MCD model is more appropriate than the power-law and TBS ones to represent the spectra of ULXs. We also tested the models which have MCD-like continua, the UC model and the broken power-law model, for IC 342 source 1, M81 X-6, and NGC 1313 source B, since their spectra have rather good photon statistics. For the latter two objects, these three models provide similar values of χ^2/ν, although the broken power-law model gives slightly lower χ^2/ν for M81 X-6. On the other hand, for IC 342 source 1, which has the highest photon statistics among the sources discussed here, the MCD model shows significantly smaller values of χ^2 than those of the other two models as shown in Table 6.1; the confidence level of the MCD, the UC, and the broken power-law model fitting is 43%, 25%, and 8%, respectively. Moreover, regardless of the source, the MCD model provides values of $N_{\rm H}$ rather consistent with the Galactic ones, whereas the other models require excess absorption, as inferred from Figure 6.26. Thus, the MCD model is best preferred.

The UC and broken power-law models are also inappropriate in view of their physical meanings. For the UC model, the obtained values of $\tau_{\rm es}$ is 20–30. Thus, the column density of the plasma, estimated by dividing the optical depth by Thomson-scattering cross-section, would amount to $\geq 10^{25}{\rm cm}^{-2}$. Since the plasma temperature is not so high, $T_{\rm e} \sim 1$ keV, the spectrum should show prominent Fe-K edge absorption feature at $\sim$7 keV, which is in fact absent in any of our ULXs spectra. Furthermore, the obtained parameters considerably contradict the necessary condition for the plasma to produce the UC emission. The UC spectrum is realized only when the emission region is "effectively thin" to free-free absorption, i.e., $\tau_{\rm eff} \sim \sqrt{\tau_{\rm ff}(\tau_{\rm ff}+\tau_{\rm es})} \ll 1$ (Rybicki and Lightman 1979), where $\tau_{\rm eff}$ and $\tau_{\rm ff}$ denote the effective and free-free optical depths, respectively. This relation, together with the obtained value of $\tau_{\rm es}$, requires quite low value of $\tau_{\rm ff}$ ($\ll 1/30$). In order for this condition to be realized down to photon energies of 0.2 keV, the plasma must have a radius of $\geq 1 \times 10^8$ cm. It seems quite artificial for such an extended plasma to be heated against the intense Compton cooling. We therefore conclude that the UC interpretation of the ULXs spectra is physically unrealistic.

Understanding the ULXs as synchrotron emission in terms of the broken power-law model is also difficult. In this regime, the break in the spectral slope is attributed to the synchrotron cooling. Our objects show relatively large breaks in photon index by 1–2, whereas a steady state synchrotron cooling predicts a break by only 0.5, which is observa-

tionally supported (e.g., Tashiro et al. 1995, Takahashi et al. 1996). Moreover, our sources take similar values of break energy, i.e., $E_{\rm bk} \sim 2.5$–3.5 keV, which is again unrealistic. For reference, the spectral breaks of blazars, determined by a balance among the electron acceleration, synchrotron cooling, and electron escape, scatter by more than three decades in energy (Kubo et al. 1998). For these reasons, the synchrotron interpretation is unlikely, too.

Thus, the MCD model is best preferred for most of the ULXs except for NGC 1313 source A in the 1993 observation and IC 342 source 2, for which the single power-law model is adequate as already mentioned in § 6.6 and § 6.8. We summarize the fitting results of the ULXs spectra in Table 7.1. It indicates that the ULXs spectra are grossly divided into two groups; one is a majority group for which the MCD model is appropriate, and the other is a minority one which can be represented by the single power-law model. As mentioned in § 2.3, the MCD emission is expected from LMXBs or BHBs. Most of ULXs have values of $T_{\rm in}$ similar to those of Galactic bright LMXBs (typically 1.5 keV), so that the LMXB interpretation is apparently preferred. However, as already described in § 2.5.3, it is difficult for LMXBs to account for the high luminosity of ULXs. In addition, the black-body component characterizing the LMXB spectra accounts for at most $\leq 30\%$ of the 0.5–10 keV fluxes for IC 342, M81 X-6, NGC 1313 source B in the 1993 observation, and NGC 4565 (when two ULXs are summed up). These are considerably lower than the black-body contribution seen in Galactic LMXBs, $\sim 50\%$ for the most luminous LMXBs (Mitsuda et al. 1984). Thus we propose that those ULXs, whose spectra can be represented by the MCD model, are accreting BHBs. The fact that some of ULXs (e.g. M33 X-8, NGC 1313 source A in the 1995 observation) show power-law hard component together with the MCD one also reinforces the BHB interpretation.

The interpretation of ULXs as MCD emission from BHBs is supported also by an astronomical point of view. As described in § 2.5.2, ULXs are generally seen in arms of spirals galaxies. Actually among our sample galaxies, M81 and IC 342 have relatively face-on geometries, and their ULXs are clearly associated with their spiral arms (see the images in Appendix C). This indicates that the ULXs belong to young population objects, and considering the time variability seen from some ULXs, compact objects associated with population I stars, e.g., the BHBs, are the most preferred candidate species.

Among our objects, two sources, i.e., NGC 1313 source A in the 1993 observation and IC 342 source 2, can be represented by the single power-law model of Γ=1.4–1.7. These values are characteristic of BHBs in the hard state. In addition, the long-term variability of NGC 1313 source A can be expressed as a soft-hard transition, as mentioned in § 6.6. Thus, all of our ULXs can be understood as BHBs, although three problems remain to be solved as mentioned below.

7.2 Problems with the BHB Interpretation

7.2.1 High BH mass to keep sub-Eddington radiation

The first problem is that very massive stellar BHs are needed to account for the high-luminosities of ULXs. In Table 7.1, we tabulated the luminosities for individual spectral components of the sample ULXs. For the power-law component, we assumed isotropic emission and calculated luminosities $L_{\rm X}^{\rm pow}$ in the 0.5–10 keV band, since this model in-

Table 7.1: Summary of the spectral fitting results of ULXs in terms of the MCD model. For NGC 1313 source A in the 1993 observation and IC 342 source 2, we adopt the single power-law model (see §6.6 and §6.8).

Source	Distance (Mpc)	Model	Γ	$f_{\rm X}^{\rm pow}$ a) (0.5–10 keV)	$L_{\rm X}^{\rm pow}$ b)	$T_{\rm in}$ (keV)	$f_{\rm bol}^{\rm disk}$ a)	$L_{\rm bol}^{\rm disk}$ c)	$R_{\rm in}$ d)
M33 X-8	0.72	MCD+PL	2.2(fix)	7.71	4.8	1.18±0.02	14.4	4.4	53^{+2}_{-3}
NGC 1313 source A	4.5								
1993 Jul.		power-law	1.69±0.05	4.13	100				
1995 Nov.		MCD+PL	$1.74^{+0.34}_{-1.02}$	1.38	33	$0.67^{+0.08}_{-0.06}$	2.33	28	390^{+50}_{-90}
NGC 1313 source B									
1993 Jul.		MCD	–	–	–	1.47±0.08	4.16	50	110±12
1995 Nov.		MCD	–	–	–	1.07±0.07	1.66	20	129^{+19}_{-16}
NGC 1365 SW source	18.3	MCD	–	–	–	$1.51^{+1.01}_{-0.47}$	0.52	100	150^{+180}_{-90}
NGC 2403 source 3	3.2	MCD	–	–	–	1.23±0.11	1.82	11	75±13
M81 X-6	3.6								
high-temp phase		MCD	–	–	–	1.59±0.09	3.92	30	72±7
low-temp phase			–	–	–	1.29±0.13	2.63	20	89^{+20}_{-15}
NGC 3628	7.7	MCD	–	–	–	$1.12^{+0.55}_{-0.41}$	0.50	18	110^{+120}_{-60}
NGC 4565	10.4								
off-center		MCD	–	–	–	1.39±0.08	1.82	117	185^{+23}_{-17}
center			–	–	–	$1.59^{+0.32}_{-0.23}$	0.72	47	89^{+28}_{-24}
Dwingeloo 1 X-1	3.0	MCD	–	–	–	$1.80^{+0.33}_{-0.26}$	1.14	6.1	26±8
IC 342	3.9								
source 1 (phase 1)		MCD	–	–	–	1.96±0.10	16.2	147	104±9
(phase 2)			–	–	–	1.50±0.10	10.3	93	142±18
(phase 3)			–	–	–	1.70±0.15	13.0	118	125^{+21}_{-18}
(phase 4)			–	–	–	1.29±0.08	7.95	72	168±20
(phase 5)			–	–	–	1.81±0.07	15.1	137	116±8
(time-average)			–	–	–	1.77±0.05	13.7	124	118±7
source 2		power-law	1.43±0.17	4.14	75				

a) In units of 10^{-12}erg s^{-1} cm^{-2}.
b) In units of 10^{38}erg s^{-1}.
b) In units of $\frac{1}{\cos i}10^{38}$erg s^{-1}.
b) $\frac{1}{\sqrt{\cos i}}$ km.

evitably needs a cut-off in low and high energies. For the MCD component, we tabulated bolometric luminosities $L_{\rm bol}$ as well as $R_{\rm in}$; the latter are calculated from equation 2.11. When the source distance D and the disk inclination i are changed, these quantities scale as

$$L_{\rm X}^{\rm pow} \propto D^2,\ L_{\rm bol}^{\rm disk} \propto D^2(\cos i)^{-1},\ R_{\rm in} \propto D(\cos i)^{-1/2}\ . \tag{7.1}$$

Hereafter we tentatively assume i=0, that makes $L_{\rm bol}^{\rm disk}$ the lowest. This assumption is not necessarily too arbitrary, since the face-on geometry provides the highest flux for a given bolometric luminosity, hence making the system more selectively detectable. Thus, many of our ULXs have luminosity $\geq 3\times10^{39}$erg s^{-1}. In order for the radiation to remain sub-Eddington, the BH mass (hereafter $M_{\rm E}$) must be quite high, typically $\geq 20\ M_\odot$. Especially for some sources whose $L_{\rm X}^{\rm pow}$ or $L_{\rm bol}^{\rm disk}$ exceed 10^{40}erg s^{-1}, such as IC 342 source 1, a quite massive BH of $M_{\rm E} \geq 70 M_\odot$ is needed.

How to make such a massive BH remains an open question, because a normal star heavier than $\sim 70 M_\odot$ is thought to be radiatively unstable, and cannot evolve to become a BH. This itself is another consequence of the Eddington limit. The bolometric luminosity of main-sequence stars scale with the mass M as

$$L = L_\odot (M/M_\odot)^{3.5} \tag{7.2}$$

where $L_\odot$=3.8$\times10^{33}$ erg s^{-1} is the bolometric solar luminosity. Thus, the bolometric luminosity of main-sequence stars, which is supplied by nuclear fusion, increases rapidly as the stellar mass increases, and at $M \sim 70 M_\odot$, L reaches $L_{\rm E}$; the star will be blown apart by its own radiation pressure.

Hence, a massive BH of $M_{\rm E} \geq 70\ M_\odot$ somewhat contradicts current understanding of the stellar evolution. However, considering the distance uncertainties and recent theoretical and observational results, this problem may not be so serious as it appears, as described in § 7.3.1.

7.2.2 Too high temperature (too small $R_{\rm in}$)

The second problem arises from the fact that the obtained values of $T_{\rm in}$ of ULXs, ranging 1.0–2.0 keV except for NGC 1313 source A, are significantly higher than those of Galactic or Magellanic BHBs (0.5–1.2 keV; e.g. Tanaka, Lewin 1995). Furthermore, as inferred from equation 2.16, a heavier BH tends to show a lower value of $T_{\rm in}$, which apparently contradicts the high $T_{\rm in}$ seen for ULXs. In other words, within our accretion-disk formalism, the BH cannot be very massive for the disk temperature to be as high as observed. In fact, substituting a typical value of $T_{\rm in}$, 1.5 keV, into equation 2.16, the mass of a Schwarzschild BH becomes only $\sim 4 M_\odot$ even if we assume η=1; then, the observed MCD luminosity would greatly exceeded the implied Eddington limit. This self-inconsistency was already pointed out by Okada et al. (1998) and Mizuno et al. (1999).

This "too-high $T_{\rm in}$ problem" may be best visualized in Figure 7.1, where our sources are plotted on $T_{\rm in}$ vs. $L_{\rm bol}$ plane, which may be called an X-ray "H–R diagram". There, dotted lines represent the loci of constant M, expressed by equation 2.13 assuming α=1, i.e. the Schwarzschild BH. Along these lines, a BH of given mass changes its $T_{\rm in}$ and $L_{\rm bol}$ obeying the relation of $L_{\rm bol} \propto T_{\rm in}^4$; both $T_{\rm in}$ and $L_{\rm bol}$ become higher as the mass accretion rate increases. On the other hand, dashed lines represent the loci of constant η, expressed by equation 2.15 (α=1). Once the luminosity normalized to the Eddington luminosity

(i.e. η) is given, a BH of higher mass tends to show lower $T_{\rm in}$ and higher $L_{\rm bol}$, obeying the relation of $L_{\rm bol} \propto T_{\rm in}^{-4}$. Thus, this Figure provides a conversion diagram from ($T_{\rm in}$, $L_{\rm bol}$) to (M, η) for non-spinning BHs within the MCD formalism. In order to consistently understand an X-ray source as an accreting non-spinning BH, the data point should fall on the region of $\eta \leq 1$ (sub-Eddington luminosity) and $M \geq 3 M_\odot$ (heavier than a NS). However, most of our ULXs (except for M33 X-8 and NGC 1313 source A) fall either on the super-Eddington region or on the $\eta \sim 1$ boundary, due to their high $T_{\rm in}$.

We can equivalently state the problem in terms of the values of $R_{\rm in}$. As expected from equation 2.8, the high values of $T_{\rm in}$ of ULXs yield relatively small values of $R_{\rm in}$. In fact, the obtained values of $R_{\rm in}$ are as small as $\sim$100 km except for NGC 1313 source A. Hence, from equation 2.10, only $\sim 10 M_\odot$ is allowed if we assume a non-spinning BH. On the contrary, the high luminosities of ULXs require $M_{\rm E}$ up to 70–100 $M_\odot$. We summarize this issue in Figure 7.2. Thus, most of our ULXs show much smaller values of $R_{\rm in}$ than are needed to account for the high luminosity. Therefore, the "too high $T_{\rm in}$ problem" can be rephrased as "too small $R_{\rm in}$ problem".

7.2.3 The change of $R_{\rm in}$

The third problem is related to the variation of $R_{\rm in}$. As reviewed in § 2.7, $R_{\rm in}$ of Galactic/Magellanic BHBs generally stays quite constant as the source varies. That is, an increase in the mass accretion rate raises the disk temperature, but does not affect the disk size. This has in turn allowed us to interpret $R_{\rm in}$ as representing the last stable orbit around the BH. It is therefore of fundamental importance to examine whether $R_{\rm in}$ of each ULX varies or not.

We have in fact detected short-term and long-term variations from three ULXs, i.e. IC 342 source 1, NGC 1313 source B, and M81 X-6. However, contrary to the case of the Galactic/Magellanic BHBs, the disk radius of all these sources exhibited negative dependences on $T_{\rm in}$; the changes are statistically significant as to the former two objects, while marginal for M81 X-6 (see § 6.2, 6.4, and 6.5). This effect is also visualized in Figure 7.1, which is drawn under the assumption of $R_{\rm in} = 3R_{\rm s}$. There, an object would vary along the dotted lines if $R_{\rm in}$ were constant like in the case of established BHBs, whereas the three ULXs actually vary along lines with a flatter slope: as the temperature becomes higher, the inferred BH mass apparently decreases, because of the decrease in $R_{\rm in}$. Clearly, this behavior is distinct from those found among the Galactic/Magellanic BHBs.

Figure 7.3 summarizes the $R_{\rm in}$ vs. $T_{\rm in}$ relations of all the three ULXs that varied. Thus, their variations approximately follow a single common scaling of $R_{\rm in} \propto T_{\rm in}^{-1}$. This effect is therefore though to reflect some fundamental difference between the ULXs and the ordinary BHBs, and the origin of this difference should be clarified. In particular, we must examine whether the variations in $R_{\rm in}$ seen from ULXs reflect real changes in the innermost disk boundary, or they are an apparent effect caused, e.g., by changes in κ. We discuss this issue in § 7.3.5.

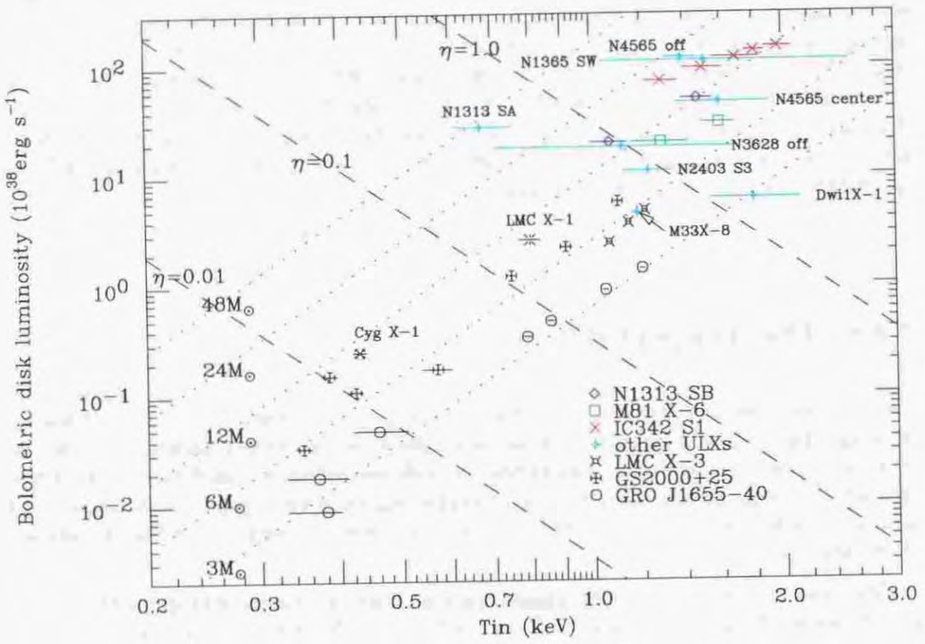

Figure 7.1: Temperature-luminosity relation of ULXs and BHBs. All the ULX datapoints refer to our *ASCA* results. For LMC X-3 and GS 2000+25, we refer to the *Ginga* results (Ebisawa 1991) for which the MCD model is employed; we discard one GS 2000+25 data point which showed the lowest flux among the *Ginga* measurement, and one LMC X-3 data point which nearly overlaps M33 X-8. The dotted lines represent the relation of $L_{\rm bol} \propto T_{\rm in}^4$ (constant mass), and the dashed lines the relation of $L_{\rm bol} \propto T_{\rm in}^{-4}$ (constant η).

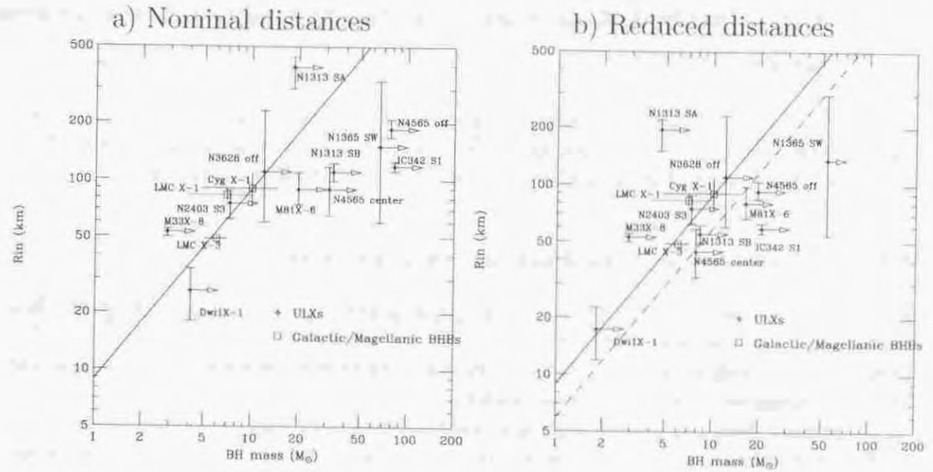

Figure 7.2: (Panel a) Relation between $R_{\rm in}$ and the BH mass, where $R_{\rm in}$ is calculated from equation 2.12, assuming ξ=0.41 and κ=1.7. The BH mass refers to $M_{\rm E}$ for ULXs, and to the optically determined mass for Galactic and Magellanic BHBs. For ULXs, we assume i=0°. The solid line represents the relation of $R_{\rm in} = 3R_{\rm S}$, which corresponds to the last stable orbit of a non-spinning BH. (Panel b) The same as panel (a), but the distances for some ULXs are reduced (see text). The dashed line effectively represents the $R_{\rm in} = 3R_{\rm S}$ relation when $\xi\kappa^2$ is increased by 50% (see text).

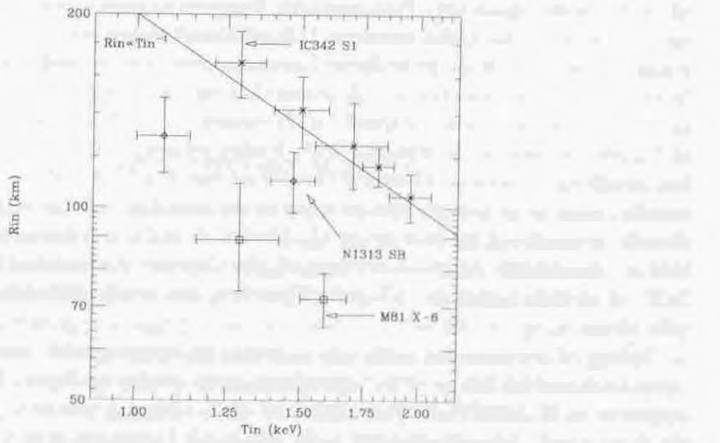

Figure 7.3: Relation between $R_{\rm in}$ and $T_{\rm in}$ for three ULXs which varied, i.e., IC 342 source 1, M81 X-6, and NGC 1313 source B. The error bars represent the 90% confidence errors tabulated in Table 7.1, and the solid line indicates the relation of $R_{\rm in} \propto T_{\rm in}$.

7.3 Possible Solutions within the Standard-Disk Framework

In order to construct a self-consistent scenario of ULXs in terms of accreting black holes, we must solve the three problems pointed out above. In this section, we attempt to do so within the framework of standard accretion disks around Schwarzschild BHs.

7.3.1 Distance and inclination uncertainties

Since the ULXs are not identified in other wavebands, we cannot estimate their disk inclinations. In addition, the distance to the host galaxy is subject to a considerable uncertainty, at least for some of them. Then, the problems (at least some of them) might be a consequence of uncertainties in i and/or D.

So far, we have somewhat arbitrary assumed i=0°, i.e., face-on geometry, for the ULXs. However, as already mentioned, this assumption makes the source luminosity the lowest. As a result, the first problem, i.e. the uncomfortably high BH mass, gets worse if i is increased. In addition, $R_{\rm in}$ scales as $\propto (\cos i)^{-1/2}$ whereas $M_{\rm E}$ scales as $\propto (\cos i)^{-1}$, as inferred from equation 7.1. As a result, the second problem (too small $R_{\rm in}$ to account for large $M_{\rm E}$) also gets worse if we increase i. Therefore, our assumption of $i = 0$ has already been adjusted to make the problems least severe.

Then, how about the source distances given in Table 7.1? We have carefully adopted these values referring to publications using various astronomical distance indicators, as summarized in Table 7.2. However, the estimates inevitably involve uncertainties; if the true distances are significantly shorter, $M_{\rm E}$ will obviously decrease in proportion to D^2. Moreover, the deviation between $R_{\rm in}$ and $M_{\rm E}$ will be relaxed, because $R_{\rm in}$ scales as $\propto D$ while $M_{\rm E}$ scales as $\propto D^2$. Therefore, the distance revision can potentially solve the first two problems. Indeed, the distances to IC 342 and Dwingeloo 1 are relatively uncertain, mainly because of their large optical extinction caused by their low Galactic latitudes. However, this does not necessarily mean that we have over-estimated their distances; in fact, the distance we have adopted for Dwingeloo 1 (3.0 Mpc) is shorter than the estimate of 5.3 Mpc based on the infrared Tully-Fisher relation (Ivanov et al. 1999). NGC 2403 has significantly more accurate distance estimates. For NGC 4565, the uncertainty is even smaller, since estimates by various authors consistently indicate ∼10 Mpc (Table 7.2) as already pointed out by Mizuno et al. (1999). Finally, the distances to NGC 1365 and M81 are accurately determined based on the Cepheid observations by HST, and that to M33, of course, is well established. Therefore, the source distances cannot be changed very much.

Taking these considerations into account, let us tentatively reduce the distances of those ULXs which fall on the "super-Eddington" region in Figure 7.1. Let us halve the distances to IC 342, NGC 1313, and NGC 4565, although this is too extreme at least for the last object. As to Dwingeloo 1, let us use 2.0 Mpc instead of 3.0 Mpc. We may also reduce the distances to NGC 1365 and M81 by 10%, within the tolerance of the HST measurements. These distance revisions modify Figure 7.2a into Figure 7.2b. There, $M_{\rm E}$ becomes relatively low, possibly consistent with the stellar evolutionary scenario, except for NGC 1365 SW source. Therefore, the first problem could be solved in this way. However, in spite of these extreme distance modifications, the revised values of $R_{\rm in}$ still

contradict $M_{\rm E}$ except for Dwingeloo-1 X-1. In short, the distance uncertainty can hardly solve the second problem, although it may affect details of the issue.

In addition, the first problem may be solved even without appealing to such extremely artificial assumptions. There are in fact fair number of observations of stars in the mass range of $\geq 100\ M_\odot$ (e.g. Krabbe et al. 1995, Walborn et al. 1995), and some authors (e.g. Fryer 1999) argue that a star heavier than $\sim 40 M_\odot$ can directly form a BH without supernova explosion (and hence without losing much of the projenitor mass). Therefore, the high BH mass may not be a big difficulty, and we do not perform further investigation of this problem.

7.3.2 Examination of the Eddington limit

Alternatively, the problems may result from our wrong application of the Eddington limit of equation 2.1, where the spherical radiation is assumed. Here, we justify the application of this equation to the case of accretion disks around BHBs, which are obviously non-spherical.

We first refer to the paper by Chen et al. (1997), who compiled observations of BH transients as well as NS transients. They collected the data of over 30 outbursts of ∼ 15 BH transients, and found the peak luminosities being distributed around 0.2 in Eddington units. Except for the two sources whose distances are relatively uncertain, none of their BH transients have shown luminosities above the Eddington limit. As to the persistent BHBs, i.e., Cyg X-1, LMC X-1, and LMC X-3, the observed luminosities have been also below $L_{\rm E}$, as described in § 7.3.4. Hence, any known BHB has luminosity below $L_{\rm E}$. Moreover, several authors theoretically show that the critical upper-limit luminosity of an axi-symmetric BH system does not differ much from the spherical one, e.g., Beloborodov (1998), Abramowicz et al. (1988), and Watarai et al. (2000). In particular, the latter two authors have shown convincingly that the disk bolometric luminosity around a stellar mass BH ($\sim 10 M_\odot$) saturate at $\sim L_{\rm E}$ even when the mass accretion rate greatly exceeds the critical values. Therefore, we can securely apply our Eddington limit of equation 2.1 on ULXs.

7.3.3 Justification of the correction factor ξ

As an alternative possibility, the problems, particularly the second one, may arise because the MCD model is not accurate enough. In particular, the second problem may be solved if the values of ξ=0.41 and κ=1.7 can take significantly lower values, because $R_{\rm in}$ scales as $\propto \xi\kappa^2$ (equation 2.11) while the disk luminosity (or $M_{\rm E}$) is independent of $\xi\kappa^2$.

Among the two parameters κ and ξ, the latter corrects the MCD formalism for the inner boundary condition of the accretion disk (see the difference between equation 2.4 and 2.6), in such a way that the disk temperature of the MCD model reaches maximum at $R_{\rm in}/\xi$ instead of $R_{\rm in}$. We can hence examine our choice of ξ=0.41 (Kubota et al. 1998) in reference to the "general relativistic accretion disk (GRAD) model" (Ebisawa et al. 1991) that properly takes into account this boundary condition as well as the relativistic effect on both the disk structure and photon trajectory.

We accordingly simulated a number of spectra using the GRAD model, by changing M, $\dot{M}$, and i, but fixing κ at 1.7. We fitted the simulated spectra with the MCD model assuming ξ=0.41, and derived the value of $R_{\rm in}$ as well as the BH mass assuming $R_{\rm in} = 3R_{\rm S}$.

Then, over the inclination range of 0° to 75° and over the disk temperature range of $T_{\rm in}$=0.5–2.0 keV, the mass obtained through the MCD analysis agreed within $\sim \pm 25\%$ with the BH mass M employed as initial inputs to the GRAD simulations, as shown in Figure 7.4. We hence conclude that our choice of ξ=0.41 properly corrects the MCD formalism for the boundary condition of the disk.

7.3.4 Comparison with Galactic/Magellanic BHBs

Even though our MCD modeling agrees with the GRAD formalism, neither model may be accurate enough to describe real celestial BHs. Furthermore, the value of κ=1.7 might be wrong. This urges us to calibrate the combined value of $\xi\kappa^2$ based on observations; for this purpose, we employ four well-studied BHBs, Cyg X-1, LMC X-1, and LMC X-3.

Dotani et al. (1997) observed Cyg X-1 with *ASCA* in 1996 May, when it was in the soft state. They analyzed the spectra assuming $D = 2.5$ kpc (Cowley 1992), and obtained parameters of $T_{\rm in} = 0.43 \pm 0.01$ keV and $R_{\rm in}\sqrt{\cos i}/\xi\kappa^2$=$71^{+13}_{-2}$ km. Together with $i = 30°$ (Cowley 1992), $\kappa = 1.7$, and $\xi = 0.41$, $R_{\rm in}$ becomes 90^{+17}_{-2} km, yielding a mass estimate of $10.2^{+1.9}_{-0.2}\ M_\odot$. This agrees well with the optically estimated value, $10.1^{+4.6}_{-5.3}\ M_\odot$ (Herreo et al. 1995). We plot the data points for Cyg X-1 on Figure 7.1 and Figure 7.2a. Thus, the choice of $\kappa = 1.7$ and $\xi = 0.41$ appears reasonable. However, a drawback in this case is that the distance to Cyg X-1 is somewhat uncertain.

LMC X-1 and LMC X-3 provide still better calibration, because their distances (50–55 kpc) are reliable; here we adopt $D = 55$ kpc. Both these Magellanic sources have been observed several times with *Ginga* by Ebisawa (1991) and Ebisawa et al. (1993), who obtained $R_{\rm in}\sqrt{\cos i}/\xi\kappa^2 = 45 \pm 3$ km and 24.5 ± 0.5 km (at 50 kpc) for LMC X-1 and LMC X-3, respectively. By substituting our assumptions of $\xi\kappa^2 = 1.18$ and $D = 55$ kpc, and assuming i=60° for LMC X-1 (Cowley et al. 1995) and i =66° for LMC X-3 (Kuiper et al. 1988), we obtain $R_{\rm in} = 83^{+6}_{-5}$ km for LMC X-1 and 49 ± 1 km for LMC X-3. Accordingly, the X-ray determined mass of LMC X-1 becomes $9.4^{+0.7}_{-0.6} M_\odot$ and that of LMC X-3 $5.5 \pm 0.1 M_\odot$. These values are consistent with the optically estimated BH mass of M=4–$10 M_\odot$ for LMC X-1 (Cowley et al. 1995) and 5–$7 M_\odot$ for LMC X-3 (Kuiper et al. 1988). We plot these two objects in Figure 7.1 and Figure 7.2a.

These calibrations utilizing Cyg X-1, LMC X-1 and LMC X-3 thus give a good support to our formalism, which assumes $\xi\kappa^2$=1.18 and the relation of $R_{\rm in} = 3R_{\rm S}$. In other words, the value of $\xi\kappa^2$ cannot be changed very much. Just to see how the "too high disk temperature problem" can be relaxed within the tolerance, let us tentatively allow $\xi\kappa^2$ to increase by 50%, although this is obviously an extreme assumption. Because the disk radius calculated by equation 2.11 is directly proportional to $\xi\kappa^2$, for all sources $R_{\rm in}$ increases by 50%. For the purpose of presentation, in Figure 7.2b we may lower the theoretical line of $R_{\rm in} = 3R_{\rm S}$ to 2/3 of the original one, instead of increasing $R_{\rm in}$ of each data point. Most of our ULXs, except for IC 342 source 1, now show relatively consistent values between $R_{\rm in}$ and $M_{\rm E}$ within errors. However, we must keep in mind that this agreement has been obtained after a series of compromising assumptions; ULXs are radiating at the Eddington limit, we observe them under the face-on geometry, and we invoke rather extreme reduction of the distance as well as the artificial 50% increase in $\xi\kappa^2$. Such extreme assumptions would not be warranted. Moreover, as a result of raising $\xi\kappa^2$ by up to 50%, the three prototypical BHBs, Cyg X-1, LMC X-1, and LMC X-3, now show discrepancy between $R_{\rm in}$ and the optically determined mass. Therefore, we conclude

that the second problem still remains essentially unsolved.

7.3.5 Constancy of $R_{\rm in}$

The comparison with the Galactic/Magellanic BHBs conducted in the previous subsection may also be utilized to investigate the third problem, i.e., the change of $R_{\rm in}$. For example, theoretical calculation by Shimura and Takahara (1995) indicates that, as $L_{\rm bol}$ approaches $L_{\rm E}$, the electron scattering effect may get severe which increases κ, e.g., from 1.7 to 1.8–2.0; then, the calculated $R_{\rm in}$ apparently decreases. To examine whether such luminosity-dependent effects are actually observed from established BHBs, we here refer again to LMC X-3, and to the BH transient GS 2000+25.

The *Ginga* observations by Ebisawa (1991) and Ebisawa et al. (1993) recorded a factor $\sim$ 3 long-term intensity variation from LMC X-3. Meanwhile, its apparent disk radius, $R_{\rm in}\sqrt{\cos i}/\xi\kappa^2$, remained constant to within $\sim$ 20%. In Figure 7.1, we plotted those *Ginga* data points of LMC X-3 for which Ebisawa (1991) performed the MCD analysis. Clearly, the data points distribute along a dotted line up to $\sim 2/3$ of the Eddington limit, without any indication of systematic change of $R_{\rm in}$. This makes a contrast to the ULX variation.

The bright BH transient GS 2000+25 is more suited for such an investigation, because of its large flux variations. Its BH mass and inclination angle have been constrained optically by several authors; M=5.9–$7.5 M_\odot$ and i=67.5–80° by Filippenko et al (1995), M=4.8–$14.4 M_\odot$ and i=43–69° by Beekman et al. (1996), and M=8.5±1.5 $M_\odot$ and i=65±9° by Callanan et al. (1996). Here, we assume i=69°.

This BH transient was observed by *Ginga* eight times spanning 240 days, covering almost the outburst peak. The obtained 2–30 keV spectra were all expressed with an MCD component plus a power-law hard tail. Importantly, the value of $R_{\rm in}\sqrt{\cos i}/\xi\kappa^2$ remained constant ($\sim 11D$ km where the source distance D is measured in kpc) within $\sim \pm 20\%$ as the intensity declined by a factor of 200 (Ebisawa 1991). With the assumption of D=3 kpc (Callanan et al. 1996), ξ=0.41, and κ=1.7, we obtain $R_{\rm in} \sim 65$ km, or $M \sim 7 M_\odot$ assuming a Schwarzschild BH. Therefore, the X-ray and optical estimates agree nicely. These *Ginga* results on GS 2000+25 are plotted also in Figure 7.1, discarding the last data point when the source was faintest. Over a wide range of $\dot{M}$ up to near the Eddington limit, the data points thus distribute along a dotted line, i.e. constant-mass ($R_{\rm in}$) grid line.

These results indicate that $R_{\rm in}$ of an ordinary BHB remains quite constant as the source varies, up to luminosities close to the Eddington limit. Therefore, the third problem, like the second one, seems specific to the ULX.

7.4 Possible Scenario to Explain ULXs

We have confirmed that the MCD formalism adequately describe the properties of Galactic/Magellanic ordinary BHBs; the standard accretion disk regime must be realized in these objects. On the other hand, due to the two distinctive features of ULXs, i.e., the higher disk temperature and the change of $R_{\rm in}$, inconsistency arises if we attempt to explain both ULXs and ordinary BHBs simultaneously under the same formalism. Therefore, ULXs are thought to be in some extraordinary physical conditions, which no longer meet our basic formalism of "standard accretion disk around Schwarzschild BHs".

Table 7.2: Summary of the adopted distances to the ULXs host galaxies and their indicators. The references are tabulated in Table 4.1

Galaxy	Distance (Mpc)	indicator
M33	0.72	–
NGC 1313	4.5	Brightest star, Largest H_{II} region, and Reduced diameter
NGC 1365	18.3	Cepheid by HST
NGC 2403	3.2	Cepheid (before HST)
NGC 3031 (M81)	3.6	Cepheid by HST
NGC 3628	7.7	Virgo inflow model
NGC 4565	10.4	Three indicators agree within 1 Mpc [a]
Dwingeloo 1	3.0	Blue band Tully-Fisher
IC 342	3.9	Virgo inflow model

[a] $10.0^{+1.5}_{-1.3}$ Mpc by the globular cluster luminosity function (Fleming et al. 1995), $10.4^{+0.4}_{-0.3}$ Mpc by the surface brightness fluctuation (Simard and Pritchet 1994), and $10.5^{+0.8}_{-1.0}$ Mpc by the planetary nebular luminosity function (Jacoby et al. 1996)

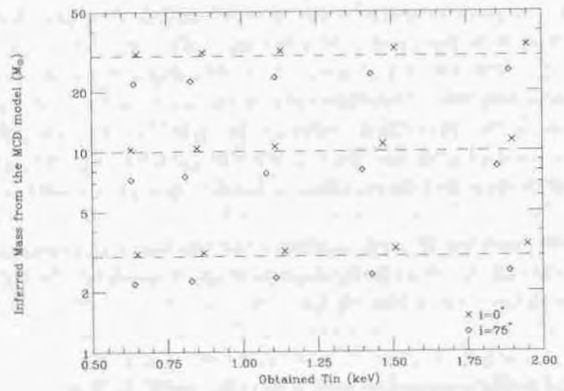

Figure 7.4: Comparison between the GRAD and the MCD model. Spectra were simulated using GRAD model of $M = 3M_\odot$, $10M_\odot$, and $30M_\odot$, by changing $\dot{M}$ and i. Obtained values of M by spectral fitting using the MCD model (assuming ξ=0.41) are plotted. Although i was changed from 0° to 75° by 15°, only the data for the two extreme values of i are plotted for clarify.

Clearly, to identify these conditions provides the clue to the nature of ULXs. With this in mind, below we attempt to explain the spectral features of ULXs, especially IC 342 source 1, M81 X-6, and NGC 1313 source B which exhibited the variation in $R_{\rm in}$.

Among the three objects, the degree of discrepancy between the obtained $R_{\rm in}$ and $M_{\rm E}$ (the value of $M_{\rm E}$ limits $R_{\rm in}$ below $3R_{\rm S} = 8.85\left(\frac{M_{\rm E}}{M_\odot}\right)$ km) is factor 2.5 for M81 X-6 (high-temperature phase spectrum), 2.7 for NGC 1313 source B (spectra in the 1993 observation), and 8.3 for IC 342 source 1 (spectra of phase 1), as inferred from Table 7.1 and Figure 7.2a. For the latter two sources, however, the distances to the host galaxies are somewhat uncertain, so that we tentatively try to explain the contradiction by a factor of ~ 3 found for M81 X-6.

7.4.1 Advection dominated accretion disk

The standard accretion disk model so far we have employed, first proposed by Shakura and Sunyaev (1973), is one of the oldest and the simplest accretion disk models. Although this model successfully explains the spectra from BHBs in the soft state, a significant progress has been achieved on the theory of accretion disks by several authors, e.g., Ichimaru (1977), Narayan and Yi (1994), Abramowicz et al. (1988), and so on. After the latest unified theory by Esin et al. (1997), the standard, optically thick, geometrically thin disk is realized in a limited range of the mass accretion rate $\dot{M}$, corresponding to $L_{\rm bol} = (0.1 - 0.5)\ L_{\rm E}$. As $\dot{M}$ becomes lower, the disk becomes optically thin, and "advection dominated accretion flow (ADAF)" occurs, where the released gravitational energy is not fully radiated away, but transported with the matter, or "advected", into the BH. On the contrary, when $\dot{M}$ increases and approaches $L_{\rm E}$, the disk becomes "optically-thick ADAF". This model was first constructed by Abramowicz et al. (1988) (see also Katz 1977, Begelman 1978), and has been studied by several authors, including Szuszkiewicz et al. (1996) and Watarai et al. (2000). Such a disk is also named a "slim accretion disk", since it is moderately geometrically-thick ($H \sim R$, where H denotes the height of the disk). In ULXs, because of their high luminosities (high $\dot{M}$), the accretion flow configuration is expected to change from the standard disk to the slim disk (optically-thick ADAF).

To be more quantitative, the rates of viscous heating, radiative cooling, and advective cooling in an accretion disk are expressed as

$$Q^+_{\rm vis} \propto \frac{\dot{M}}{R^3}\ ,\ Q^-_{\rm rad} \propto \frac{\dot{M}^{1/2}}{R^3\Sigma^{1/2}}\ ,\ Q^-_{\rm adv} \propto \frac{\dot{M}^2}{R^{7/2}\Sigma}\quad , \tag{7.3}$$

(Kato et al. 1998), where Σ denotes the surface mass density. The term "advective cooling" means that entropy is carried away by the radial infall of the accreting matter. Thus, the energy released via viscosity ($Q^+_{\rm vis}$) is balanced by radiative cooling ($Q^-_{\rm rad}$) when $\dot{M}$ is small (standard disk regime), whereas balanced by advective cooling ($Q^-_{\rm adv}$) when $\dot{M}$ is high (slim disk regime). This is the reason why the slim accretion disk is realized when $\dot{M}$ is high.

Although the spectrum emergent from a slim disk is a superposition of local black-body radiation like in the case of a standard accretion disk, it differs from the standard-disk spectrum in the following three points (e.g., Watarai et al. 2000):

1. When the advective cooling becomes important, some portion of the released energy

is no longer radiated away. As a result, the disk luminosity does not much exceed $L_{\rm E}$, even when $\dot{M}$ becomes very high (called super-critical accretion).

2. As $\dot{M}$ increases, advective energy transport becomes the dominant cooling process, especially at inner disk regions. As a result, the effective temperature profile flattens, from $T_{\rm eff} \propto R^{-3/4}$ (equation 2.6) to $T_{\rm eff} \propto R^{-1/2}$ at the extreme.

3. The X-rays are radiated not only from the regions outside the last stable orbit, but also from the region inside it. Watarai et al. (2000) fitted the numerically calculated disk spectrum by the MCD model (both $R_{\rm in}^{\rm MCD}$ and $T_{\rm in}$ are the model parameters), and found that as $\dot{M}$ increases, $R_{\rm in}^{\rm MCD}$ decreases while $T_{\rm in}$ increases. The relation between $R_{\rm in}^{\rm MCD}$ and $T_{\rm in}$ in this stage is roughly approximated as $R_{\rm in}^{\rm MCD} \propto T_{\rm in}^{-1}$ (hence, $R_{\rm in} \propto T_{\rm in}^{-1}$). Then, the bolometric disk luminosity approximately scales as

$$L_{\rm bol} \propto R_{\rm in}^2 T_{\rm in}^4 \propto T_{\rm in}^2 \propto R_{\rm in}^{-2} \ . \tag{7.4}$$

Thus, by presuming that the slim disk is realized in ULXs, the "change of $R_{\rm in}$" problem, approximately expressed as $R_{\rm in} \propto T_{\rm in}^{-1}$, can be explained quantitatively by item 3. Furthermore, item 1 ensures that the emergent luminosity stays close to $L_{\rm E}$ even if $\dot{M}$ changes largely, which in turn justifies our assumption that the highest luminosity observed from each source is close to $L_{\rm E}$.

Because the slim disk has a smaller $R_{\rm in}$ and a higher $T_{\rm in}$ (item 3) than a standard disk of the same parameters, it can also qualitatively explain the "too high $T_{\rm in}$ problem", or the "too small $R_{\rm in}$ problem". Let us below examine whether this idea can *quantitatively* explain the factor 3 discrepancy in the $R_{\rm in}/M_{\rm in}$ ratio exhibited by our ULXs. In Figure 7.1, the slim-disk scaling ($R_{\rm in} \propto T_{\rm in}^{-1}$) of each variable ULX holds over a typical range from the observed highest luminosity $L_{\rm max}$ (which we tentatively identify with $L_{\rm E}$) down to $\sim L_{\rm max}/2$. Equation 7.4 then predicts that $R_{\rm in}$ at the brightest occasion should be at least $\sqrt{2}$ time smaller than would be expected if the source is in the standard-disk regime. In this way, the slim disk scenario can explain the $R_{\rm in}/M_{\rm in}$ discrepancy by up to a factor of ~ 1.5. However, in order to fully resolve the factor 3 discrepancy, the source must make a transition from the standard-disk to slim-disk regimes at still lower luminosities, e.g., $L_{\rm bol} = \frac{1}{3^2} L_{\rm E} \sim 0.1 L_{\rm E}$. This contradicts the results presented in § 7.3.5, where the standard accretion disk picture has been confirmed to be valid up to $\sim \frac{2}{3} L_{\rm E}$ in the case of GS 2000+25 and LMC X-3.

The above difficulty is enhanced by recent discoveries of several Galactic BH transients with high values of $T_{\rm in}$, including GRO J1655-40 (Zhang et al. 1997, Ueda et al. 1998), GRS J1915+15 (Belloni et al. 1997), and 4U 1630-47 (Oosterbroeck et al. 1998). In particular, the mass and inclination of the Galactic jet source GRO J1655-40 have been determined accurately as $M = 7.0 \pm 0.2\ M_\odot$ and $i = 69.^\circ5 \pm 0.^\circ08$ (Orosz and Bailyn 1997). Thus, the GRO J1655-40 system is very similar to GS 2000+25 and LMC X-3 both in the BH mass and the inclination. According to the *Rossi X-ray Timing Explorer* (*RXTE*) measurements (Méndez et al. 1998) during the 1995 August outburst, the flux of GRO J1655-40 decreased by almost two orders of magnitude, whereas $R_{\rm in}\sqrt{\cos i}/\xi\kappa^2$ remained almost constant (typically 25 ± 1 km). We plot all these *RXTE* data in Figure 7.1, assuming $D = 3.2$ kpc (Hjellming and Rupen 1995), ξ=0.41 and κ=1.7. Because $R_{\rm in}$ thus remained constant and the luminosity was considerably below $L_{\rm E}$, the source cannot have been in the slim-disk regime. Nevertheless, $T_{\rm in}$ of this jet source is ~ 1.5 times

higher that that of GS 2000+25 when compared at the same luminosity. This makes the X-ray determined mass of GRO J1655-40, $\sim 3\ M_\odot$, fall much short of the optical mass ($7\ M_\odot$). Thus, the same "too high $T_{\rm in}$" problem is observed from a BH system that is in the standard-disk regime rather than in the slim-disk condition.

In summary, the $R_{\rm in} \propto T_{\rm in}^{-1}$ relation seen in ULXs can be solved adequately by the slim-disk scenario. However, the same idea can give only a partial solution to the "too high $T_{\rm in}$" problem. The remaining part of this issue must therefore be attributed to some physical conditions that is not related to $\dot{M}$, but intrinsic to the BH itself. In other words, there may be two types of BHs. One type comprises ordinary Galactic/Magellanic BHBs, and obey the standard-disk scenario up to a relatively high luminosity close to $L_{\rm E}$. The other type of objects, including ULXs and the high-$T_{\rm in}$ BH transients, exhibit rather high disk temperature, and display the slim-disk effects when the luminosity approaches $L_{\rm E}$. Then, our remaining task is to identify the origin of the difference between these two types of BHs.

7.4.2 Spinning BH scenario

A BH can be characterized only by three fundamental parameters; the mass M, electrical charge, and the angular momentum J. When it becomes an X-ray source via mass accretion, additional two parameters come in; the mass accretion rate $\dot{M}$ and the system inclination i. Out of these five system parameters, we have fully taken M, $\dot{M}$ and i into account already. Then, the difference between the two types of BHs (previous subsection) should be attributed either to the electric charge or the angular momentum. Considering that the universe is very close to electrical neutrality, the only possibility is the angular momentum. In fact, real BHs in the universe may well have considerable angular momenta, even though we have so far assumed non-spinning (i.e. Schwarzschild) BHs for simplicity. For example, massive stars are usually fast rotators, and their collapse will produce spinning BHs described by the Kerr solution. Below, we examine whether the remaining issues can be solved by considering Kerr BHs.

Hereafter, we express the BH angular momentum J in a dimensionless manner, i.e., by a spin parameter $a_* \equiv \frac{c}{GM^2} J$. This parameter takes values between -1 to 1; $a_* = 1$ means the extreme Kerr hole for a prograde disk (i.e., rotating in the same direction as the BH), $a_* = -1$ also represents the extreme Kerr hole but for a retrograde disk, and $a_* = 0$ corresponds, of course, to the Schwarzschild BH.

The most immediate effect of the BH spin is that it affects the radius of the last stable orbit, $R_{\rm last}$, as (e.g. Berdeen et al. 1972)

$$R_{\rm last} = \frac{R_{\rm S}}{2} \left\{ 3 + Z_2 \mp [(3 - Z_1)(3 + Z_1 + 2Z_2)]^{1/2} \right\} \ , \tag{7.5}$$

where $Z_1 = 1 + (1 - a_*^2)^{1/3} \left[(1 + a_*)^{1/3} + (1 - a_*)^{1/3} \right]$, $Z_2 = (3a_*^2 + Z_1^2)^{1/2}$, and the lower and upper signs are for a prograde disk and a retrograde disk, respectively. We here pay attention only to the prograde disk, since in this case $R_{\rm last}$ (hence $R_{\rm in}$) decreases as a_* increases, as shown in Figure 7.5a. Thus, a prograde accretion disk around a Kerr hole has a smaller $R_{\rm in}$, and consequently a higher $T_{\rm in}$, suggesting that the BH spin can explain the problem with ULXs. This idea has first been proposed by Zhang et al. (1997) to explain the observed high temperature of GRS 1915+105 and GRO J1655-40.

Neglecting relativistic effects for the moment, we can perform simple quantitative estimates. If we start from a Schwarzschild BH and increase its spin, with M and $\dot{M}$ kept constant, then $R_{\rm last} = R_{\rm in}$ decreases from $3R_{\rm S}$ down to $\frac{1}{2}R_{\rm S}$ as the BH approaches the extreme Kerr hole (Figure 7.5a). This implies a factor 6 decrease in $R_{\rm in}$. Meanwhile, the value of $T_{\rm in}$, which scales as $R_{\rm in}^{-3/4}$ (equation 2.6), becomes higher by a factor of $\left(\frac{1}{6}\right)^{-3/4} = 3.8$. Even taking a somewhat less extreme case of $a_* = 0.95$, we expect $R_{\rm last} = R_{\rm in}$ to decrease by a factor of 3 compared to the Schwarzschild BH case. This is apparently sufficient to explain the discrepancy between $R_{\rm in}$ and $M_{\rm E}$ seen in ULXs, although relativistic effects are yet to be considered (see next subsection).

Assuming BH spin has another merit, that the radiative efficiency, defined as $L_{\rm bol}/\dot{M}c^2$, gets higher as the BH angular momentum increases. The efficiency is 0.057 for a Schwarzschild case, while it increases up to 0.42 for an extremely Kerr hole (e.g. Kato et al. 1998). Therefore, for a rapidly rotating BH, the same mass accretion rate can produce 5 times higher luminosity than in a non-spinning BH, although the same Eddington limit should still apply.

A Kerr BH has yet another important property. As shown by Beloborodov (1998), an optically-thick accretion disk around a Kerr BH tends to be more advective than that around a Schwarzschild one. Accordingly, we expect an optically-thick disk around a Kerr hole to make a transition into a slim disk at a considerably lower luminosity than the Schwarzschild case. This successfully answer the question which has arisen in the previous section; "why the slim disk seems to occur preferentially among ULXs, whereas not realized in ordinary BHBs?"

From these considerations, we propose that the ordinary Galactic/Magellanic BHs (Cyg X-1, LMC X-1, LMC X-3, GS 2000+25, and so on) have insignificant angular momenta ($|a_*| << 1$), while ULXs and high-$T_{\rm in}$ Galactic transients (e.g. GRO J1655-40) involve Kerr BHs with prograde accretion disks. This may solve the overall issues associated with ULXs in the following manner. Firstly, the BH spin reduces $R_{\rm in}$ and raises $T_{\rm in}$ according to Figure 7.5a. Secondly, the BH spin enhances the slim-disk condition, which in turn adds to the decrease in $R_{\rm in}$ and increase in $T_{\rm in}$ (see previous subsection). Finally, the induced slim disk condition explains the observed $R_{\rm in} \propto T_{\rm in}^{-1}$ relation. In the next subsection, we confirm that this final scenario is valid even when taking relativistic effects into account.

7.4.3 Spectra from accretion disks around Kerr BHs

The X-ray spectra emergent from an accretion disk is subject to several relativistic corrections, due to gravitational redshift, transverse and longitudinal Doppler shifts, and gravitational focusing. To a distant observer, both the observed color temperature and flux will deviate from the local values, depending on the inclination angle i and the BH spin.

We first examine the effects of the gravitational and transverse Doppler redshifts of a face-on disk. The ratio of the photon energy observed at infinity (E_o) and at the disk surface (E), when viewed from $i = 0°$, is given as (e.g., Cunningham et al. 1975, Asaoka

1989),

$$\frac{E_{\rm o}}{E} = \frac{\sqrt{1 - \frac{3}{2}\left(\frac{R_{\rm S}}{R}\right) + \frac{a_*}{\sqrt{2}}\left(\frac{R_{\rm S}}{R}\right)^{3/2}}}{1 + \frac{a_*}{2\sqrt{2}}\left(\frac{R_{\rm S}}{R}\right)^{3/2}} . \quad (7.6)$$

We calculated the energy ratio at $R = (7/6)^2 R_{\rm last}$, where the disk temperature becomes maximum (§ 2.7), and show the results in Figure 7.5b. Thus, a face-on disk suffers strong gravitational and transverse redshifts, which becomes severer as a_* increases. These effects are so strong that the increase in the local disk temperature, caused by the decrease in $R_{\rm in}$ in Kerr BHs, is almost canceled out. Therefore, a nearly face-on geometry is not favored. When i increases, however, the longitudinal Doppler effects start increasing the $E_{\rm o}/E$ ratio, and hence the disk color temperature becomes higher.

To examine the overall relativistic effects, more detailed numerical calculations of the emergent spectra are needed. Such calculations have already been performed by several authors, including Cunningham et al. (1975), Asaoka (1989), and Zhang et al. (1997). They in fact showed that, although the spectrum from an optically-thick accretion disk around a Kerr BH is similar in shape to that around a Schwarzschild one, the color temperature of the spectrum and the integrated flux are strongly dependent on a_* and i. Here we show the spectra of $a_* = 0$ and $a_* = 0.998$ (Schwarzschild and nearly extreme Kerr hole respectively) calculated by Cunningham et al. (1975) in Figure 7.6. The latter value of a_* is that at which a black hole will equilibrate with the disk accretion (Throne 1974). They calculated the expected spectra for each viewing angle considering the relativistic effects based on their "transfer function", which represents the relative intensity of the ray, emitted from each portion of the disk surface to the observer, as a function of i and R. As seen in Figure 7.6, the color temperature of the spectra strongly depends on i for a rapidly rotating BH, and a spectrum harder than that in the Newtonian potential is expected when viewed relatively edge-on.

Their results have been confirmed by Zhang et al. (1998) by using the same transfer functions. These authors represent the relativistic effects by two correction factors. One is the change of the color temperature denoted $\kappa_{\rm GR}$, due to the gravitational redshift and Doppler red/blue-shifts ($T_{\rm col}/T_{\rm eff} \propto \kappa_{\rm GR}$). The other is the change of the flux denoted $g(i, a_*)$, due to the viewing geometry and the gravitational focusing ($f_{\rm X} \propto \frac{1}{g}$ instead of $f_{\rm X} \propto \frac{1}{\cos i}$ in the Newtonian case). Because we expect $M_{\rm E} \propto L \propto \frac{1}{g}$ and $R_{\rm in} \propto \sqrt{\frac{L}{(T_{\rm eff})^4_{\rm in}}} \propto \frac{\kappa_{\rm GR}^2}{\sqrt{g}}$, the quantity $R_{\rm in}/M_{\rm E}$ scales with $\kappa_{\rm GR}^2\sqrt{g}$. Figure 7.7 give this combined correction factor, $\kappa_{\rm GR}^2\sqrt{g}$, for a Schwarzschild and a nearly-extreme Kerr holes. To get a true value of $R_{\rm in}/M_{\rm E}$, we must multiply this correction factor to the apparent value of $R_{\rm in}/M_{\rm E}$ derived through the MCD fit to the data assuming an $i = 0$ standard disk around a Schwarzschild BH.

Thus, if we assume a Kerr BH of a_*=0.998, and view the disk from an inclination angle of $i \geq 65°$, the correction factor exceeds ~ 2. When this is combined with another factor of ~ 1.5 due to the slim-disk property (§ 7.4.1), we can explain the discrepancy by a factor of 3 between $R_{\rm in}$ and $M_{\rm E}$. Since $i \sim 60°$ is what is expected on average when the disks are randomly oriented, the chance probability of finding such objects is reasonably high. For those ULXs of which the $R_{\rm in}$ vs. $M_{\rm E}$ discrepancy is smaller, e.g. Dwingeloo-1 X-1, NGC 2403 source 3 and NGC 3628 off-center source, even a Kerr hole which is closer to the face-on geometry can give adequate explanation. Obviously, M33 X-8 and NGC 1313

source A can be explained even without invoking the slim disk or BH rotation, since they originally fall on the sub-Eddington regime in Figure 7.1.

We conclude that the mystery of ULXs can be solved in terms of the slim accretion disk and the BH rotation.

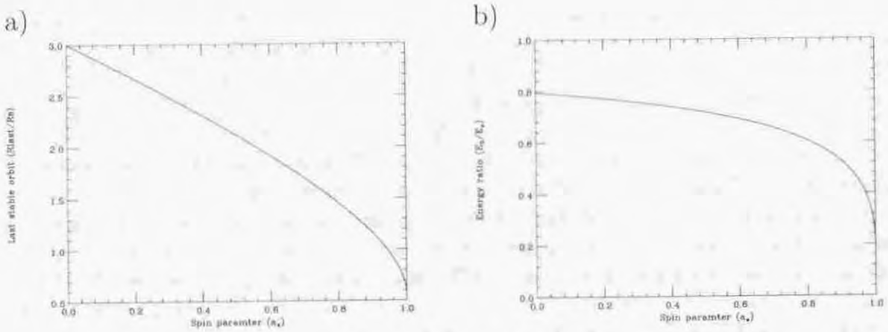

Figure 7.5: (a) Radius of the last stable orbit as a function of a_* for a prograde disk. (b) The ratio off the energy observed at infinity (E_o) and the disk surface (E) as a function of a_*, calculated at $R = \frac{49}{36} R_{\rm last}$, where the temperature of the standard disk becomes maximum.

7.4.4 Formation of a massive spinning BH

We end this chapter by discussing how to make a massive, rapidly rotating BH. In short, there seems to exist at least three possibility to make a Kerr BH of 50–100 $M_\odot$. One is a simple, straight-forward scenario, that a massive rotating star collapses into a massive BH. Another needs two ordinary stellar-mass BHs; if they come close and merge into a single BH, it would have a doubled mass, and inherit the angular momentum from the orbital motion. The other is expected in XRBs, where the BH is spun up by the accreting matter, and obtain both the mass and angular momentum.

As already quoted in § 7.3.1, Fryer (1999) show that a massive star of $\geq$40 $M_\odot$ will directly form a BH, without experiencing a supernova explosion. We also refer here to Nakamura et al. (1987), who showed through numerical simulations that the gravitational collapse of a rotating massive star usually produces a rather extreme Kerr hole, without exhibiting the naked singularity. Thus, among the three scenarios presented above, the first one is particularly preferred since it can naturally explain the difference between the ordinary stellar-mass BHBs and ULXs. When a BH in the ordinary mass range ($\sim 10 M_\odot$) is formed through supernova explosion, a large amount of mass, hence a large amount of angular momentum of the projenitor star, will be lost into the expanding supernova ejecta. On the other hand, a very massive star will form a BH without losing much of its mass and angular momentum. Thus, if the value of the initial angular momentum is sufficient, a rapidly rotating, massive BH would be born. If this BH tidally traps another ordinary star and forms a close binary, a ULX is realized.

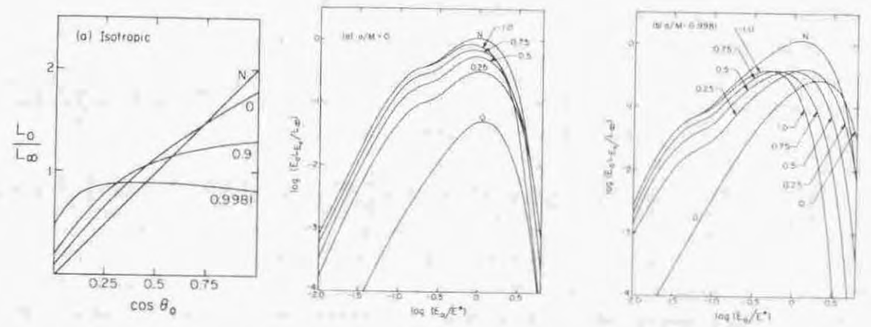

Figure 7.6: Relativistic effects on the disk spectrum, taken from Cunningham (1975). (Left) The inclination dependence of the flux. Numbers along the lines indicate the values of a_*, and θ_0 is the inclination. The straight line denoted "N" corresponds to the case under the Newtonian potential. (Middle) The expected spectra of the disk around a Kerr hole of $a_* = 0$, with the values denoting $\cos i$. "N" is the spectrum under the Newtonian potential seen from $i = 0°$. (Right) The same as the middle panel, but for a case of $a_* = 0.998$.

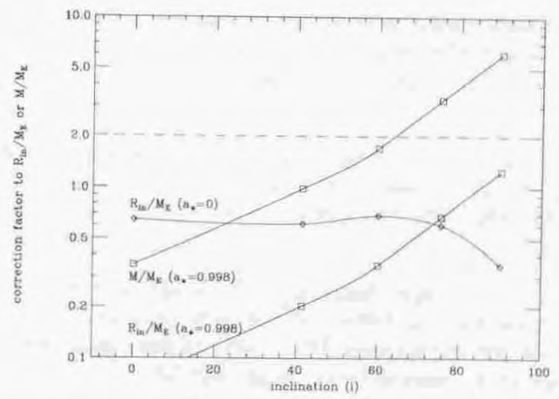

Figure 7.7: Correction to $R_{\rm in}/M_E$ or $M/M_{\rm E}$, calculated based on the correction factor of Zhang et al (1997). The line of $M/M_{\rm E}$ includes the reduction of $R_{\rm in}$.

In order to examine this scenario, we briefly estimate the spin of a BH formed directly from a massive star. For this purpose, let us calculate the angular momentum of the sun, regarding it as a rigid rotator, as: $\frac{2}{5} f M_\odot R_\odot^2 \dot{\phi} = 9.5 \times 10^{41} f$ kg m^2 s^{-1} where $R_\odot$=7$\times 10^8$ m is the solar radius, $M_\odot$=2 $\times$ 10^{30} kg is the solar mass, $\dot{\phi} \sim \frac{2\pi}{30 \text{ day}}$ is angular velocity of the solar rotation, and f is a form factor representing the mass concentration ($f = 1$ means that the internal mass density is uniform). Considering $f \sim 0.18$, the solar angular momentum is in fact comparable to the maximum angular momentum $J_{\max}$ for a $1M_\odot$ BH, $\frac{GM_\odot^2}{c} = 8.9 \times 10^{41}$ kg m^2 s^{-1}.

Thus, even for the sun which is a slow rotator, $\frac{J}{J_{\max}}$ reaches of order unity. Since the radius of main-sequence stars is scaled as $R \propto M^{3/4}$, the ratio $\frac{J}{J_{\max}} \propto \frac{R^2}{M}\dot{\phi} \propto M^{1/2}\dot{\phi}$. Therefore a massive star, which tends to have higher angular velocity than the sun, would be expected to form into a nearly extremely Kerr BH in the case of the direct collapse.

Further discussion on the formation scenario of heavy stellar-mass Kerr holes, however, is beyond the scope of the present thesis.

Chapter 8

SUMMARY AND CONCLUSION

Using *ASCA*, we have observed twelve ULXs in nine spiral galaxies, and three X-ray luminous SNRs for comparison. By analyzing these *ASCA* data and partially utilizing those from the *ROSAT* HRI, we have obtained the following new results.

1. Our objects are basically point-like, and four of them showed intensity variations. These results reinforce the interpretation of ULXs as high-luminosity single objects.

2. The spectra of the three SNRs have been confirmed to be distinct from those of the ULXs. Consequently, ULXs cannot be interpreted as young SNRs, but are considered to be accreting compact objects.

3. Out of the twelve ULX spectra, nine can be described with a single MCD model, one with a power-law plus MCD model, and two with a single power-law model. Since these spectra are typical of BHBs, it is indicated that the ULXs are mass-accreting black holes, where the MCD emission arises from optically-thick accretion disks.

4. The observed bolometric luminosity of the MCD emission is distributed over 10^{39-40} erg s^{-1}. For these luminosities to remain sub-Eddington, relatively high BH masses up to $\sim 100\ M_\odot$ are required. This provides an observational evidence that very massive stellar BHs exist.

5. From the three variable ULXs, we have detected characteristic changes in the accretion-disk radius, which are roughly expressed as $R_{\rm in} \propto T_{\rm in}^{-1}$. This can be interpreted as one of first observational evidences for the optically-thick ADAF that has been theoretically predicted.

6. The disk temperature of the ULXs is unusually high at $T_{\rm in}$=1.0–1.8 keV. Consequently, the disk radius $R_{\rm in}$ is $\sim$ 100 km, which is too small to account for the inferred high BH mass (item 4). The ADAF scenario can explain this problem partially, but not completely. We have shown that the issue can be solved if in addition the BHs are spinning rapidly, because the last stable orbit gets closer to the BH in a Kerr BH than in a Schwarzschild BH, and the accretion disk can get hotter even considering the relativistic effects. Thus, based on firm physical grounds, we have for the first time given a unified interpretation to the long-lasting mystery of ULXs.

Reference

Abramowicz M.A., Czerny B., Lasota P., Szuszkiewicz E. 1988, ApJ 332, 646

Alexander S.G., Mészáros P. 1991, ApJ 372, 554

Asaoka I. 1989, PASJ 41, 763

Bardeen J.M., Press W.H., Teukolsky S.A. 1972, ApJ 178, 347

Beekman G., Shahbaz T., Naylor T., Charles P.A. 1996, MNRAS 218, L1

Begelman M.C. 1978, MNRAS 184, 53

Beloborodov A.M. 1998, MNRAS 297, 739

Belloni T., Méndez M., King A.R., van der Klis M., van Paradjis J. 1997, ApJ 479, L145

Boese G. 1998, The ROSAT Point Spread Function and Associates, available online via http://wave.xray.mpe.mpg.de/exsas/documentation/tech_reports

Bregman J.N., Cox C.V., Tomisaka K. 1993, ApJ 415, L79

Bregman J.N., Schulman E., Tomisaka K. 1995, ApJ 439, 155

Brandt W.N., Halpern J.P., Iwasawa K. 1996, MNRAS 281, 687

Callanan P.J., Garcia M.R., Filippenko A.V., McLean I., Teplitz H. 1996, ApJ 476, L57

Carignan C., Côté S., Freeman K.C., Quinn P.J. 1997, AJ 113, 1585

Carral P., Hollenbach D.J., Lord S.D., Colgan S.W., Michael, R.H. Rubin R.H., Erickson E.F. 1994, ApJ 423, 223

Chen W., Shrader C.R., Livio M. 1997, ApJ 491, 312

Clark G., Doxsey R., Jernigan F.Li.J.G., Van Paradijs J. 1978, ApJL 221, 37

Colbert J.M., Petre R., Schlegel E.M., Ryder S.D. 1995, ApJ 446, 177

Cowley A.P. 1992, ARA&A 30, 287

Cowley A.P., Schmidtke P.C., Anderson A.L., Mcgrath T.K. 1995, PASP 107, 145

David L.P., Harnden F.R., Kearns K.E., Zombeck M.V., Harris D.E., Mossman A.E., Prestwich A., Primini F.A., et al. 1999 October, The ROSAT High Resolution Imager (HRI) Calibration Report, U.S. ROSAT Science Data Center/SAO.

Dubus G., Charles P.A., Long K.S., Hakara P.J. 1997, ApJL 490, 47

Ebisawa K., 1991, PhD Thesis, University of Tokyo

Ebisawa K., Mitsuda K., Hanawa T. 1991, ApJ 367, 213

Ebisuzaki T., Hanawa T., Sugimoto D. 1984, PASJ 36, 551

Esin A., McClintock J.E., Narayan R. 1997, ApJ 489, 865

de Vaucouleurs G. 1963, ApJ 137, 720

de Vaucouleurs G. 1979, AJ 84, 1270

de Vaucouleurs G., de Vaucouleurs A., Corwin H.G., Buta R.J., Paturel G., Fouqué P. 1991, Third Reference Catalogue of Bright Galaxies (New York: Springer)

Fabbiano G. 1989, ARA&A 27,87

Fabbiano G. 1988, ApJ 325,544
Fabbiano G., Trinchieri G. 1984, ApJ 286, 491
Fabbiano G., Trinchieri G. 1987, ApJ 315, 46
Fabbiano G., Trinchieri G., Van Speybroeck L.S. 1987, ApJ 316, 127
Fabbiano G., Heckman T., Keel W.C. 1990, ApJ 355, 442
Fabbiano G., Kim D.-W., Trinchieri G. 1992, ApJS 80, 531
Fabbiano G., Juda J.Z. 1997, ApJ 476, 666
Fleming D.E.B., Harris W.E., Pritchet C.J., Hanes D.A. 1995, AJ 109, 1044
Flippenko A., Matheson T., Barthe A.A. 1995, ApJ 455, L139
Freedman W.L., Madore B.F. 1988, ApJL 332, 63.
Freedman W.L., Hughes S. M., Madore B.F., Mould J.R., Lee M.G., Stetson P., Kennicutt R.C., Turner A. et al. 1994, ApJ 427, 628
Fukazawa Y., Ishida M., Ebisawa K. 1997, ASCA News No.5, 3
Fryer C.L. 1999, ApJ 522, 413
Giacconi R., Gursky H., Paolini F., Rossi B. 1962, Phys. Rev. Letters 9, 439
Giacconi R., Branduardi G., Briel U., Epstein A., Fabricant D., Feigelson E., Forman W., Gorenstein P. et al. 1979, ApJ 230, 540
Gioia I.M., Maccacaro T., Schild R.E., Stocke J.T., Liebert W., Danziger I.J., Kunth D., Lub J. 1984, ApJ 283, 495
Hjellming R.M., Rupen M.P. 1995, Nature 375, 464
Heckman T.M. 1980, A&A 87, 152
Hechkan T.M., Balick B., Crane P.C. 1980, A&AS 40, 295
Houck J.C., Bregman J.N., Chevalier R.A., Tomisaka K. 1998, ApJ 493, 431
Ho L.C., Filippenko A.V., Sargent W.L.W. 1997, ApJS 112, 315
Holt S.S., Gotthelf E.V., Tsunemi H., Negoro H. 1994, PASJ 46, L151
Hummel E., Sancisi R., Ekers R.D. 1984, A&A 133,1
Hummerl E., Dettmer R.J., Wielebinski R. 1986, A&A 166,97
Ichimaru S. 1977, ApJ 214, 840
Inoue H., Koyama K., Makishima K., Matsuoka M., Murakami T., Oda M., Ogawara Y., Ohashi T., et al. 1981, ApJ 250, L71
Israel F.P. 198, A&A 194,24
Ishisaki Y., Makishima K., Iyomoto N., Hayashida K., Inoue H., Mitsuda K., Tanaka Y., Uno S. et al. 1996, PASJ 48, 237
Ishisaki Y. 1996, PhD thesis, University of Tokyo
Iyomoto N. 1999, PhD Thesis, The University of Tokyo.
Iyomoto N., Kakishima K., Fukazawa Y., Tashiro M., Ishisaki Y. 1997, PASJ 49, 425
Ivanov V.D., Alonso-Herrere A., Rieke M.J., McCarthy D. 1999, ApJ 118, 826
Jacoby G.H., Ciardullo R., Harris W.E. 1996 ApJ, 462, 1
Kato S., Fukue J., Mineshige S. 1998, Black-Hole Accretion Disks (Kyoto University Press, Kyoto)
Katz J.I. 1977, ApJ 215, 265
Kaneda T. 1988, PhD Thesis, The University of Tokyo, ISAS RN 642
Keel W.C. 1983, ApJ 269, 466

Kitamoto S., Tsunemi H., Miyamoto S., Hayashida K. 1992, ApJ 394, 609
Kohmura et al. 1994, PASJ 46, L157
Kohmura Y. 1994, PhD Thesis, The University of Tokyo
Kormendy J. 1988, ApJ 335, 40
Komossa S., Schulz H. 1998, ApJ 339, 345
Koyama K., Ikeuchi S., Tomisaka K. 1986, PASJ 38, 503
Koyama K., Petre R., Gotthelf R., Hwang E.V., Matsuura M., Ozaki M., Holt S.S. 1995, Nature 378, 255
Kraan-Korteweg R.C., Loan A.J., Burton W.B., Lahav O., Fergusson H.C., Henning P.A., Lynden-Bell D. 1994, Nature 372, 77
Krabbe A., Genzel R., Eckart A., Najarro F., Lutz D., Cameron M., Kroker H., Tacconi-German L.E., Thatte N. et al. 1995, ApJ 447, L95
Kubo H., Takahashi T., Madejski G., Tashiro M., Makino F., Inoue S., Takahara F. 1998, ApJ 504, 693
Kuiper L., van Paradijs J., van der Klis M. 1988 A&A 203, 79
Long K.S., D'Odorico S., Charles P., Dopita M.A. 1981, ApJ 246, L61
Long K.S., Van Speybroeck L.P. 1983, in Accretion-Driven X-Ray Sources, ed W. Levin, E.P.J. van den Heuvel (Cambridge University Press) p117
Lorre J.J. 1978, ApJL 222, L99
Makishima K., Maejima Y., Mitsuda K., Brandt H.V., Remillard R.A., Tuohy I.R., Hoshi R., Nakagawa M. 1986, ApJ 308, 635
Makishima K., Ohashi T., Hayashida K., Inoue H., Koyama K., Takano S., Tanaka Y., Yoshida A., et al. 1989, PASJ 41, 697
Makishima K., Fujimoto R., Ishisaki Y., Kii T., Loewenstein M., Mushotzky R., Serlemitsos P., Sonobe T. et al. 1994, PASJ 46, L77
Makishima K., Tashiro M., Ebisawa K., Ezawa H., Fukazawa Y., Gunji S., Hirayama M., Idesawa E. et al. 1996, PASJ 48, 171
Makishima K., Mihara T., Nagase F., Tanaka Y. 1999, ApJ 525, 978
Markert T.H., Rallis A.D. 1983, ApJ 275, 571
Méndez M., Belloni T., van der Klis M. 1998, ApJ 499, L187
Marrison R., McCammon D. 1983, ApJ 270, 119
Masai K. 1984, Ap&SS 98, 367
Matsumoto H., Tsuru G.T. 1999, PASJ 51, 321
Mewe R., Gronenschild E.H.B.M., van den Oord G.H.J. 1985, A&AS 62,197
Miller S., Schlegel E.M., Petre R., Colbert E. 1998, ApJ 116, 1657
Misra T., Melia F. 1997, ApJ 484, 848
Mitsuda K., Inoue H., Koyama K., Makishima K., Matsuoka M., Ogawara Y., Shibazaki N., Suzuki K. et al. 1984, PASJ 36, 741
Mitsuda K., Inoue H., Nakamura N., Tanaka Y. 1989, PASJ 41, 97
Mizuno T., Ohnishi T., Kubota A., Makishima K., Tashiro M. 1999 PASJ 51, 663
Morse J.A. 1994, PASP 106, 675
Nagase F. 1989, PASJ 41, 1
Nakamura N., Dotani T., Inoue H., Mitsuda K., Tanaka Y. 1989, PASJ 41, 617
Nakamura T., Oohara K., Kojima Y. 1987, Prog. Theor. Phys. Suppl. 90, 1

Narayan R., Yi I. 1994, ApJ 428, L13

Novikov I.D., Throne K.S. 1973, in Black Hole, ed. DeWitt C., DeWitt B. (Gordon & Breach, New York) p343

Okada K., Dotani T., Makishima K., Mitsuda K., Mihara T. 1998, PASJ 50, 25

Ohashi T., Koyama K., Makishima K., Matuoka M., Murakami T., Oda M., Ogawara Y., Shibazaki N., et al. 1982 ApJ 258, 254

Ohasi T., Ebisawa K., Fukazawa Y., Hiyoshi K., Horii M., Ikebe Y., Ikeda H., Inoue H., et al. 1996, PASJ 48, 157

Oosterbroek T., Parmar A.N., Kuulkers E., Belloni T., van der Klis M., Frontera F., Santangelo A. 1998, A&A 340, 431

Orosz J.J., Bailyn C.D. 1997, ApJ 477, 876; erratum 482, 1086

Page D.N., Thorne K.S. 1974, ApJ 191, 499

Palumbo G.G.C., Fabbiano G., Fransson C., Trinchieri G. 1985, ApJ 298, 259

Petre R., Okada K., Mihara T., Makishima K., Colbert E.J.M. 1994, PASJ 46, L115

Read A.M., Ponman T.J., Strickland D.K. 1997, MNRAS 286, 626

Reynolds C.S., Loan,A.J., Fabian A.C., Makishima K., Brandt W.N., Mizuno T. 1997, MNRAS 286, 349

Rice W., Lonsdale C.J., Soifer B.T., Neugevauer G., Kopan E.L., Lloyd L.A., De Jong T., Habing H.J. 1988, ApJS 68, 91

Raymond J.C., Smith B.W. 1977, ApJS 35, 419

Rybicki G.B., Lightman A.P. 1979, *Radiative Processes in Astrophysics* (New York: Wiley and Sons, Inc.)

Ryder S., Steveley-Smith L., Dopita M., Petre R., Colbert E., Malin D., Schlegel E. 1993, ApJ 416, 167

Rupen M.P., Van Gorkom J.H., Knapp G.R., Gunn J.E., Schneider D.P. 1987, AJ 94, 61

Sanwal D., Robinson E.L., Zhang E., Colomé C., Harvey P.M., Ramseyer T.F. 1996, ApJ 460, 437

Serlemitsos P.J. 1981, NASA Tech. Mem. 83848, 441

Serlemitsos P.J. 1988, Appl. Opt. 27, 1447

Serlemitsos P.J., Jalota L., Soong Y., Kunieda H., Tawara Y., Tsusaka Y., Suzuki H., Sakima Y. et al. 1995, PASJ 47, 105

Sérsic J.L., Pastoriza M. 1965, PASP 77, 287

Schlegel E.M. 1994, ApJ 424, L99

Schulman E., Bregman J.N. 1995, ApJ 441,568

Shakura N.I., Sunyaev R.A. 1973, A&A 24, 337

Silbermann N.A., Harding P., Ferrarese L., Stetson P.B., Madore B.F., Kennicutt R.C., Freedman W.L., Mould J.R. et al. 1999, ApJ 515, 1

Simard L., Pritchet C.J. 1994, AJ 107, 503

Smith D.A., Neff S.G., Bothun G.D., Fanelli M.N., Offenberg J.D., Waller W.H., Bohlin R.C., O'Connell R.W., et al. 1996, ApJ 473, L21

Soifer B.T., Sanders D.B., Madore B.F., Neugebauer G., Danielson G.E, Elias J.H., Lonsdale C.J., Rice W.L. 1987, ApJ 320, 238

Stetson R.B., Saha A., Ferrarese L., Rawson D.M., Ford H.C., Freedman W.L., Gibson B.K., Graham J.A. et al. 1998, ApJ 508, 491

Szuskiewicz E., Matthew A., Malkan A., Abramowicz M.A. 1996, ApJ 458, 474

Takano M., Mitsuda K., Fukazawa Y., Nagase F. 1994, ApJ 436, L47

Takahashi T., Tashiro M., Madejski G., Kubo H., Kamae J., Kataoka J., Kii T., Makino F. et al. 1996, ApJ 470, L89

Tanaka Y. 1989 in: *Two Topics in X-ray Astronomy*, 23rd ESLAB Symp., Bologna, Italy (ESA, Paris), p.3

Tanaka Y., Inoue H., Holt S.S. 1994, PASJ 46, L37

Tanaka Y., Lewin W. H. G. 1995, in X-ray Binaries, ed W. H. G. Lewin, J. van Paradijs, W. P. J. van den Heuvel (Cambridge University Press, Cambridge) p126

Tammann G.A., Sandage A. 1968, ApJ 151, 825

Tashiro M., Makishita K., Ohashi T., Inda-Koide M., Yamashita A., Mihara T., Kohmura Y. 1995, PASJ 47, 131

Telesco C.M., Gatley I. 1984, ApJ 284, 557

Terashima Y., Ptak A., Fujimoto R., Itoh M., Kunieda H., Makishima K., Serlemitsos P.J. 1998, ApJ 496, 210

Throne K.S. 1974, ApJ 191, 507

Toor A., Seward F.D. 1974, A.J. 79, 995

Trinchieri G., Fabbiano G. 1985, ApJ 290, 96

Trinchieri G., Fabbiano G., Peres G. 1988, ApJ 325, 531

Trinchieri G., Fabbiano G., Palulumbo G.G.C. 1985, ApJ 290, 96

Trinchieri G., Fabbiano G., Romaine S. 1990, ApJ 356, 110

Tsuru T. 1992, PhD Thesis, The University of Tokyo, ISAS RN 528

Tsuru G.T., Awaki H., Koyama K., Ptak A. 1997, PASJ 49, 619

Ueda Y., Inoue H., Tanaka Y., Ebisawa K., Nagase F., Kotani T., Gehrels N. 1998, ApJ 492, 782

Veron P., Lindblad P.O., Zuiderwijk E.J., Veron M.P., Adam G. 1980, A&A 87, 245

Volger A., Pietsch W., Kahabka P. 1996, A&A 305, 74

Yaqoob T., Serlemitsos P.J., Ptak A., Mushotzky R., Kunieda H., Terashima Y. 1995, ApJ 455, 508.

Ueda Y. 1996, PhD thesis, University of Tokyo

Uno S. Annual Meeting of Astronomical Society of Japan, 1996 Spring, R40a

Uno S. 1997, PhD Thesis, Gakushuin University

Walborn N.R., Long K.S., Lennon D.J., Kudritzki R.P. 1995, ApJ 454, L27

Watson M.G., Stanger V., Griffiths R.E. 1984, ApJ 286, 144

Watarai K., Fukue J. Mineshige S. 2000, PASJ, in press.

Worrall D.M., Marshall F.E., Boldt E.A., Swank J.H. 1982, ApJ 255,111

White N.E., Stella L., Parmar A.N. 1988, ApJ 324, 363

Zhang S.N., Ebisawa K., Sunyaev R., Ueda Y., Harmon B.A., Sazonov S., Fishman G.J., Inoue H. et al. 1997, ApJ 479, 381

Appendix A

Spectral model descriptions

Here we briefly explain the spectral models used in this thesis.

Power-law model This is the simplest, and widely used model, mainly representing non-thermal emission as was seen in AGNs, X-ray pulsars, and so on. The photon flux per unit energy is expressed as

$$f(E) = K \left(\frac{E}{1 \text{ keV}} \right)^{-\Gamma} , \tag{A.1}$$

where K is the normalization factor and Γ is the photon index, which we assume to be positive in general. Obviously,, this draws a straight line in the logalithmic plot, as shown in Figure A.1a.

TBS model An optically this hot plasma of temperature T radiates photons due to the process called bremsstrahlung or free-free emission; photons are radiated from accelerated electrons in the Coulomb fields of ions. The spectrum is obtained by integrating the radiation over thermally distributed electrons, so that we call the emission "thermal bremsstrahlung (TBS)". The emissivity is written as

$$\varepsilon_\nu^{ff} = 6.8 \times 10^{-38} Z^2 n_e n_i T^{-1/2} e^{E/kT} \bar{g}_{ff} \text{ erg s}^{-1} \text{ cm}^{-3} \text{ Hz}^{-1} , \tag{A.2}$$

where Z and n_i are the charge and number density of ions, n_e is the number density of electrons, and $\bar{g}_{ff}$ is the Gaunt factor (Rybicki and Lightman 1979). In the X-ray band, $\bar{g}_{ff} \sim E^{-0.4}$. Therefore in the low energy range the spectrum is similar in shape to a power-law model of photon index $\Gamma \sim 1.4$, whereas at $E \gg kT$, flux drops sharply as shown in Figure A.1c.

Raymond-Smith plasma emission model In addition to the continuum emission as described by a TBS model, a thin hot plasma shows atomic emission lines of heavy elements through collisional excitations, as shown in Figure A.1c. The center energy and equivalent width of each line depend on the abundance of the relevant element and temperature of the plasma. Although there exists several plasma emission codes (Raymond and Smith 1977, Masai 1984, Mewe et al. 1985), we use only Raymond-Smith model in this thesis, since none of objects in our sample show strong emission lines and the obtained results are almost independent of the plasma codes.

MCD model As described in § 2.7, the MCD model is an approximation of the emission from optically-thick, geometrically-thin accretion disks (Shakura and Sunyaev 1973, Mitsuda et al. 1984, Makishima et al. 1986). The spectrum is a superposition of black-body radiations from individual portions of the disk. Integrating from the innermost disk radius $r_{\rm in}$ to the outermost disk radius $r_{\rm out}$, and assuming $r_{\rm in} \ll r_{\rm out}$, we obtain the spectrum as

$$f(E) = \frac{\cos i}{D^2} \int_{r_{\rm in}}^{r_{\rm out}} 2\pi r B(E,T) dr = \frac{8\pi r^2 \cos i}{3D^2} \int_{T_{\rm out}}^{T_{\rm in}} (\frac{T}{T_{\rm in}})^{-11/3} B(E,T) \frac{dT}{T_{\rm in}} \quad , \quad \text{(A.3)}$$

where i is a inclination angle of the disk, D is the distance to the source, and $T_{\rm in}$=$T(r_{\rm in})$ and $T_{\rm out}$=$T(r_{\rm out})$ are the innermost and outermost disk temperature, respectively. The spectrum is approximated by a single temperature black-body radiation at high energy and drops sharply, whereas in the low energy range it resembles in shape a power-law of $\Gamma = -2/3$, as shown in Figure A.1d.

Unsaturated Comptonization (UC) model This model is realized when hot thermal electrons of a plasma Compton up-scatter some seed photons, but do not saturate to the Wien peak spectrum for most photons. The spectrum is characterized by an electron temperature, $T_{\rm e}$, and an optical depth for electron scattering, $\tau_{\rm es}$. In the high-energy range, i.e., over the electron temperature, the spectrum drop off sharply. On the other hand, the low-energy continuum has power-law like shape whose slope is determined by the combination of $T_{\rm e}$ and $\tau_{\rm es}$. Thus, when $T_{\rm e}$ is close to $T_{\rm in}$ of the MCD model and $\tau_{\rm es}$ is optimized, this model is almost identical to the MCD one in spectral shape, and can equally represent the soft component of LMXBs or BHBs in the soft state, as described in White et al. (1988) and Ebisawa et al. (1991).

Broken power-law model This is an empirical model to represent the spectrum of a rather convex shape, and written as

$$f(E) = \begin{cases} K \left(\frac{E}{1\ {\rm keV}}\right)^{-\Gamma_1} & E \leq E_{\rm bk} \\ K \left(\frac{E_{\rm bk}}{1\ {\rm keV}}\right)^{\Gamma_2-\Gamma_1} \left(\frac{E}{1\ {\rm keV}}\right)^{-\Gamma_2} & E \geq E_{\rm bk} \end{cases} \quad , \quad \text{(A.4)}$$

where $E_{\rm bk}$ is the break-point energy, while Γ_1 and Γ_2 represent the photon indices below and above $E_{\rm bk}$, respectively. As shown in Figure A.1 this model and the UC model resemble the MCD model when parameters are appropriately selected.

Photo-electric absorption At low energies, X-ray emission suffers absorption by cold matter between the source and the observer. The absorber can be either local to the source, associated with the host galaxy, or attributed to the interstellar medium within our Galaxy. The effect of the absorption on the incident spectrum $f(E)$ is expressed as

$$f'(E) = f(E) \times e^{-N_{\rm H}\sigma(E)} \quad , \quad \text{(A.5)}$$

where $\sigma(E)$ is the cross section of photo-electric absorption assuming cosmic abundances for the absorber (Marrison and McCammon 1983) and $N_{\rm H}$ is equivalent hydrogen column density. Although $N_{\rm H}$ represents the number of hydrogen atoms per unit area, hydrogen does not contributes much to the absorption. Instead, in

the energy range of 0.5–2 keV that is related to us, the absorption is mainly caused by K-shells of O, Ne, Mg, Si, and S, as well as L-shell of ion. We show an absorbed power-law model in Figure A.1d.

(a) Power-law

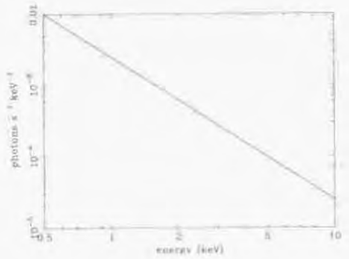

(b) Power-law with absorption

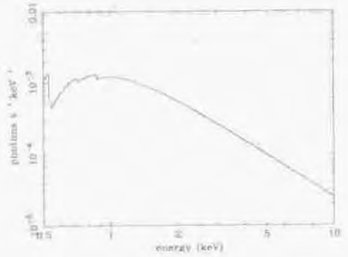

(c) R-S plasma emission

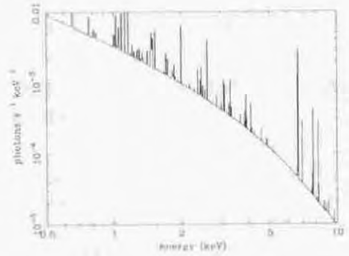

(d) MCD

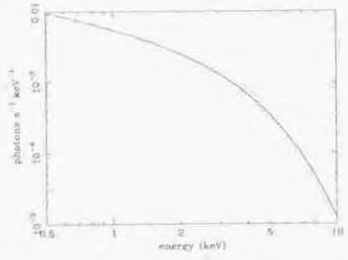

(e) UC

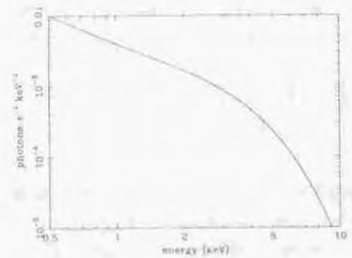

(f) Broken power-law

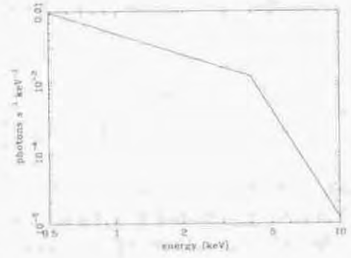

Figure A.1: Examples of typical spectral models. (a) A power-law of photon index Γ=2. (b) An absorbed power-law of photon index Γ =2. We assume $N_{\rm H}$=1×10^{21} cm^{-2}. (c) A Raymond-Smith model of a thin-hot plasma, with the temperature kT=3 keV and the abundance of one solar. We can see emission lines, superposed on the continuum which is almost identical in shape with that of TBS model of the same temperature. (d) An MCD model of $T_{\rm in}$=1 keV. This model shows the most convex shape among our models. (e) An UC model of $T_{\rm e}$=1 keV and $\tau_{\rm es}$=30. The shape of this model is similar to that of the MCD model. (f) A broken power-law model of Γ^1=1, Γ^2=5, and $E_{\rm bk}$=4 keV. This empirical model can also represent the MCD-like convex shape.

Appendix B

Calibration of the *ASCA* spectral response

The spectral response of *ASCA* has been calibrated based on both the pre-launch experiments and the in-orbit calibrations, and is best adjusted on the 1-CCD nominal position, where the source is located near the center of S0C1. Observations of bright, well-known Galactic X-ray sources have been utilized for the calibration of the GIS (plus the XRT) response; the instrumental parameters of the GIS and XRT (e.g., the energy dependence of the energy resolution of the GIS, optical constants associated with the XRT, and so on) have been adjusted within the ground-calibration tolerance, so that the observed spectra of the calibration targets can be well reproduced by a physically reasonable model spectrum. Among the calibration objects, the Crab Nebula is regarded as a standard one and its spectrum is known to be expressed with an absorbed power-law model with Γ = 2.08–2.11 and $N_{\rm H}$ = (0.27–0.33) × 10^{22} cm^{-2} (Toor & Seward 1974). As already described by Makishima et al. (1996) and Fukazawa et al. (1997), the current response functions are so well determined that the high-quality spectrum of the Crab Nebula can be fitted by the model consistent with that of Toor & Seward (1974) for both the GIS 2 and GIS 3, and the fit residuals is only ∼1%. To confirm this, we fitted the Crab spectra obtained in September 1994, when the source was observed at the 1-CCD nominal position, by an absorbed power-law model with all the model parameters independent between the GIS 2 and GIS 3. We obtained a marginally good fit (χ^2/ν=719/458), with the parameters of $\Gamma = 2.078 \pm 0.003$ and $N_{\rm H} = (0.299 \pm 0.003) \times 10^{22}$ cm^{-2} for GIS 2, and $\Gamma = 2.078 \pm 0.003$ and $N_{\rm H} = (0.280 \pm 0.003) \times 10^{22}$ cm^{-2} for GIS 3; hence both results are consistent with those of Toor & Seward (1974). The dead-time corrected normalizations between the two sensors agree with each other within 3%. Although the spectral fit performed above is statistically unacceptable and there extists an artificial winding in the fit residuals as shown in Figure B.1a, the degree of the deviations from the best-fit model is within ∼ ±1.5%. Therefore we regard this 1.5% as a typical measure of the calibration uncertainty of the GIS (plus the XRT) spectral response concerning the spectral shape.

Since the SIS suffers telemetry saturation when it observes the Crab Nebula, the cross-calibration between the SIS and the GIS has been performed by observing moderately bright sources, and the SIS response has been adjusted to produce the results consistent with those of the GIS. We present the SIS/GIS spectra of 3C273 obtained on the 1-CCD nominal position in Figure B.1b, and fitted them with a power-law plus TBS models (the latter describes soft excess). We constrained the spectral parameters to be common

between the SIS and GIS, and obtained an acceptable fit (χ^2/ν=238/209). Although the model normalizations are left free between these two instruments, they turned out to be consistent within 3%. Studies performed by the instrumental team based on the observations of various sources (including 3C273) indicate that the relative normalization among the four detectors (SIS 0, SIS 1, GIS 2, and GIS 3) agree within ∼5%, and the other spectral parameters are indistinguishable in most cases within the fitting errors. Therefore we estimate the SIS (plus the XRT) spectral response uncertainty to be as small as that of the GIS plus the XRT with respect to the spectral shape.

Although the *ASCA* spectral response is thus well calibrated at the nominal position, the results may depend on the source position. Such studies have been done by Fukazawa et al. (1997), based on the GIS spectra of the Crab Nebula acquired at various focal-plane positions. As shown in Figure B.2, model normalizations scatter rather largely up to ∼10%, whereas the values of photon index Γ, which denote the spectral hardness of the source, change within only ∼ ±0.05 depending on the source position. In summary, the observing position has a noticeable influence only on the source flux.

(a) (b)

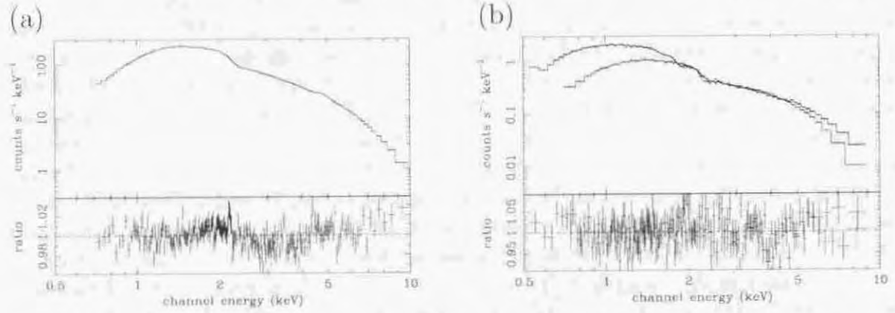

Figure B.1: *ASCA* spectra of X-ray bright sources. Panel (a) is the GIS 2 spectrum of the Crab Nebula, fitted with a power-law model with absorption, and panel (b) is the SIS/GIS spectra of 3C273, jointly fitted by a power-law plus TBS models, with only the relative normalization left free between the two spectra. Both sources are observed on the 1-CCD nominal position.

(a) (b)

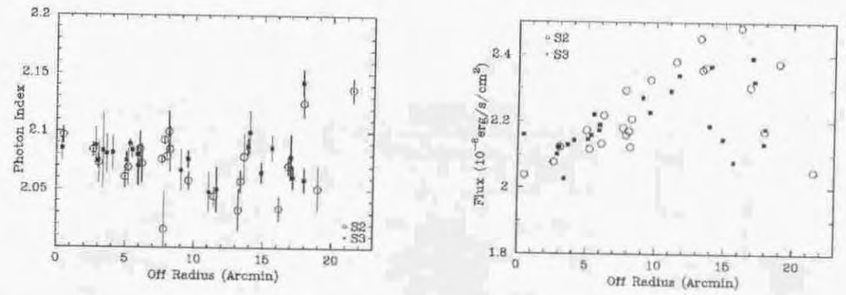

Figure B.2: The best-fit parameters of the Crab spectra obtained at different focal-plane positions, taken from Fukazawa et al. (1997). Photon index Γ (panel a) and the 2–10 keV flux after a dead-time correction (panel b) are plotted as a function of the distance from the optical axis.

Appendix C

X-Ray Images of the Sample Galaxies

We present X-ray contours of our sample galaxies superposed on the optical (Digital Sky Survey) image. The *ASCA* images are taken in the 0.5–10 keV band for both the SIS and the GIS. X-rays are smoothed with a gaussian distribution of $\sigma = 0.'05$, $0.'1$, and $0.'5$ for the HRI image, the SIS image, and the GIS image, respectively.

M33 HRI

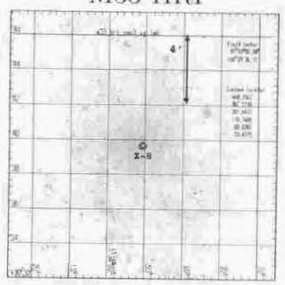

M33 SIS

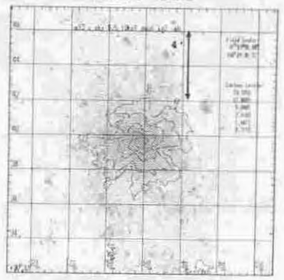

M33 GIS

NGC 891 HRI

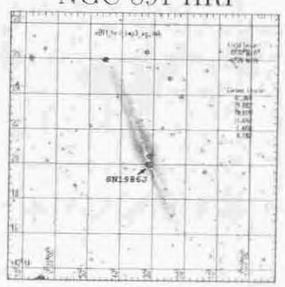

NGC 891 SIS

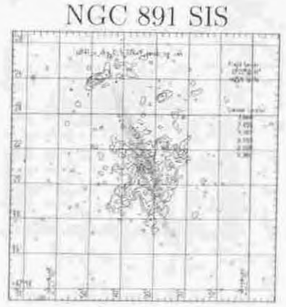

NGC 891 GIS

NGC 1313 HRI

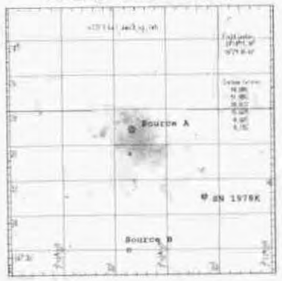

NGC 1313 SIS

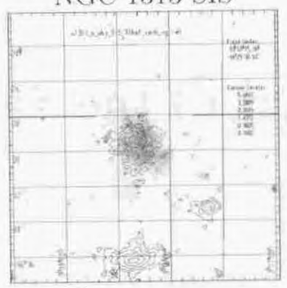

NGC 1313 GIS

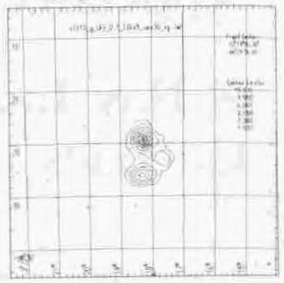

NGC 1365 HRI

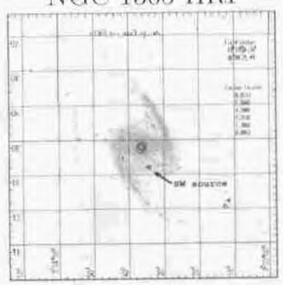

NGC 1365 SIS

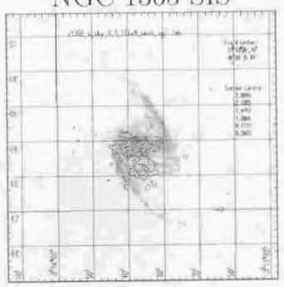

NGC 1365 GIS

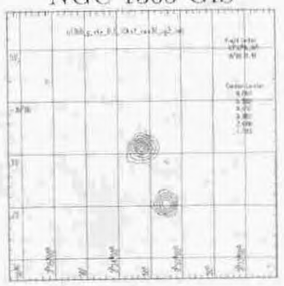

NGC 2403 HRI

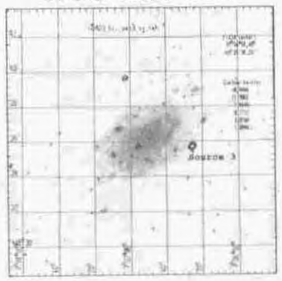

NGC 2403 SIS

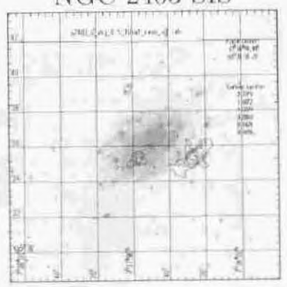

NGC 2403 GIS

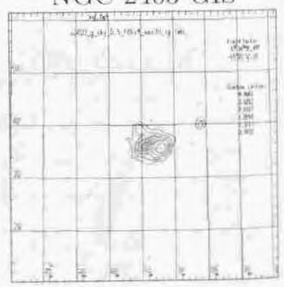

M81 HRI

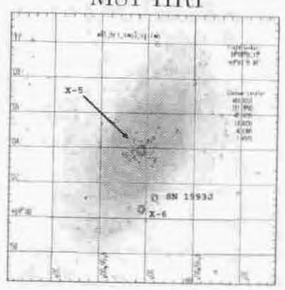

M81 SIS

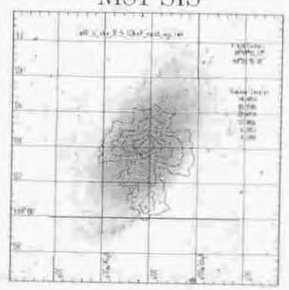

M81 GIS

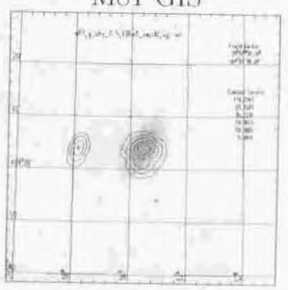

NGC 3628 HRI

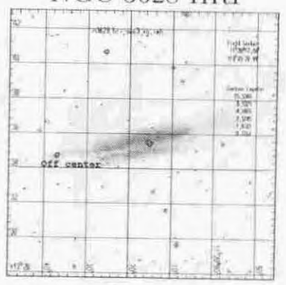

NGC 3628 SIS

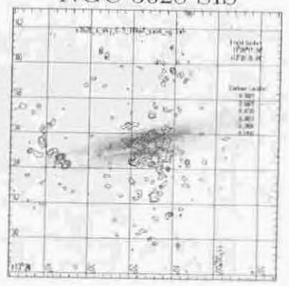

NGC 3628 GIS

NGC 4565 HRI

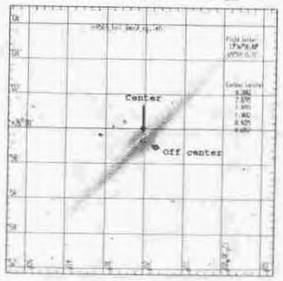

NGC 4565 SIS

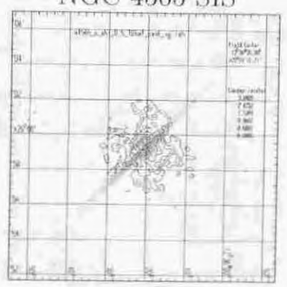

NGC 4565 GIS

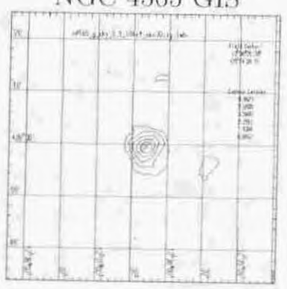

NGC 6946 HRI

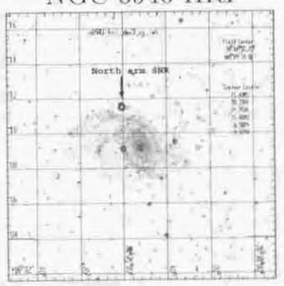

NGC 6946 SIS

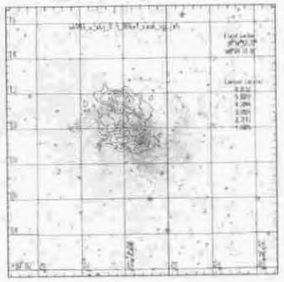

NGC 6946 GIS

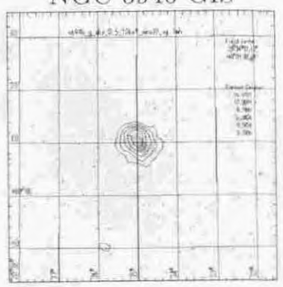

IC 342 HRI

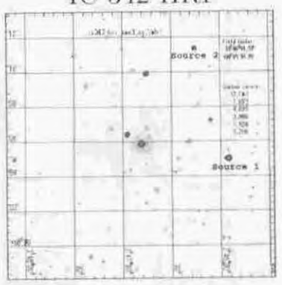

IC 342 SIS

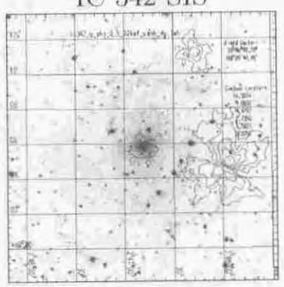

IC 342 GIS

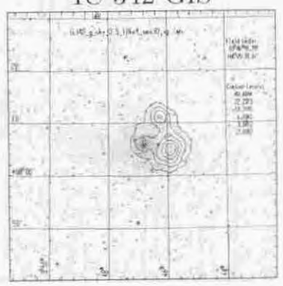

Dwingeloo 1 SIS

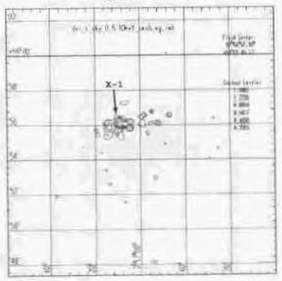

Dwingeloo 1 GIS

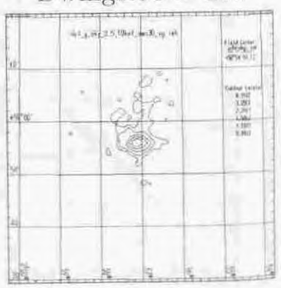

Appendix D

Light Curves of ULXs

We summarize the ULX (and SNR) light curves obtained by *ASCA* in the 0.5–10 keV energy range, including background. The typical background count rate is 0.02 and 0.01 c s^{-1} for the SIS and the GIS, respectively. Each light curves is tested against a constant-intensity hypothesis, and the assumed count rate is represented in the figure as a horizontal straight line. For some sources, only the SIS (or the GIS) light curve is shown (see § 5.2).

M33 pos1 SIS

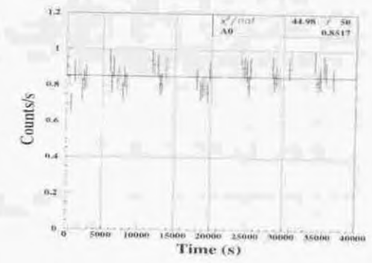

M33 pos1 GIS

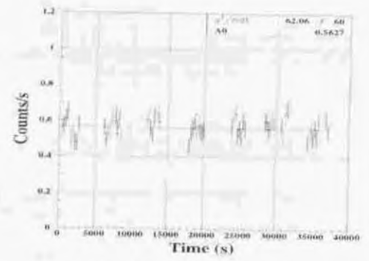

M33 pos2 SIS

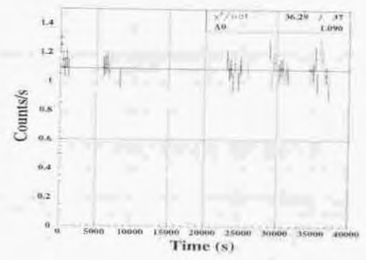

M33 pos2 GIS

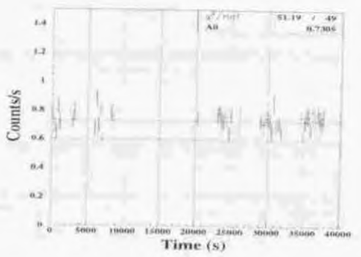

SN 1986J 94/01 SIS

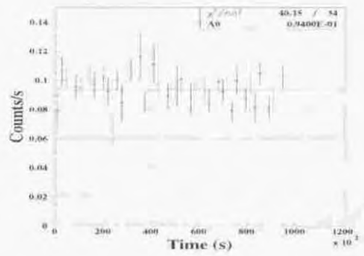

SN 1986J 94/01 GIS

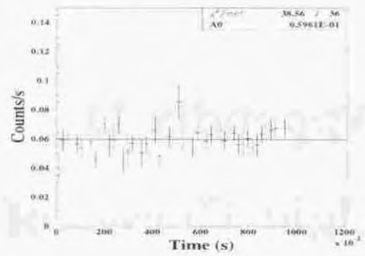

SN 1986J 96/01 SIS

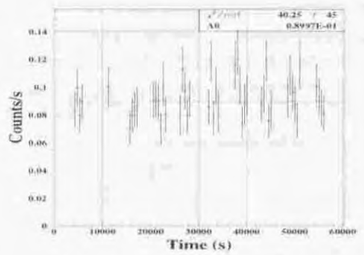

SN 1986J 96/01 GIS

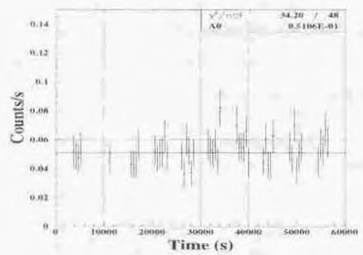

N1313 SA 93/07 SIS

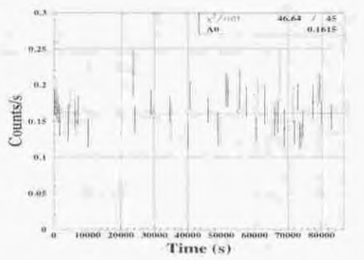

N1313 SA 93/07 GIS

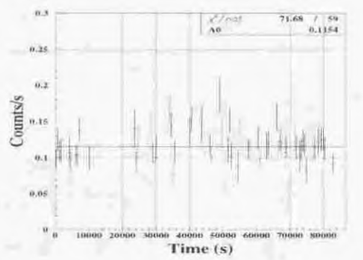

N1313 SB 93/07 SIS

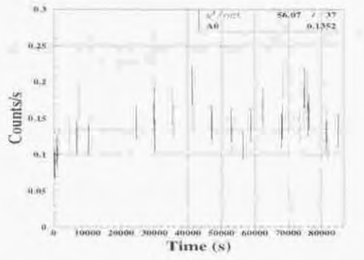

N1313 SB 93/07 GIS

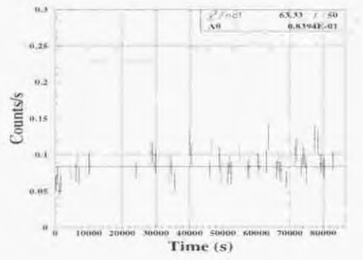

SN 1978K 93/07 SIS

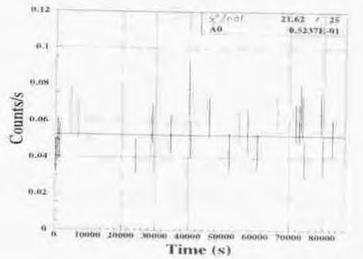

SN 1978K 93/07 GIS

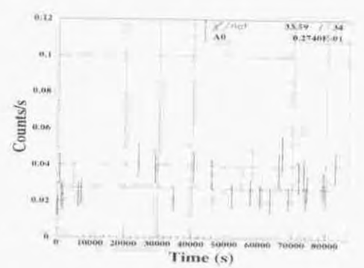

N1313 SA 95/11 SIS

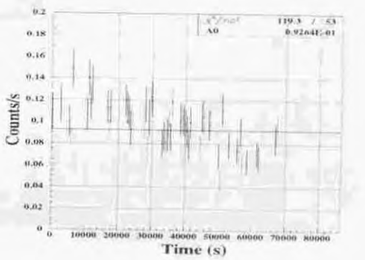

N1313 SA 95/11 GIS

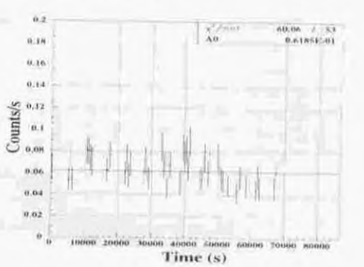

N1313 SB 95/11 SIS

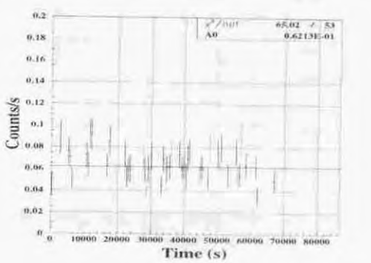

N1313 SB 95/11 GIS

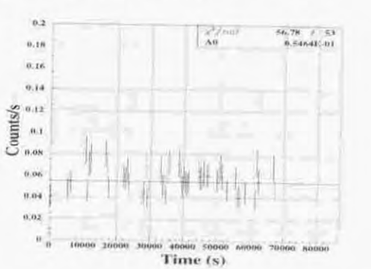

SN 1978K 95/11 SIS

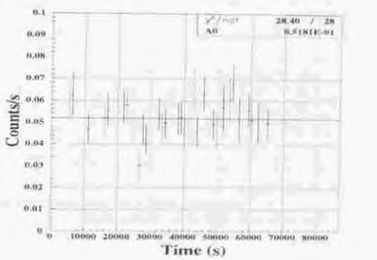

SN 1978K 95/11 GIS

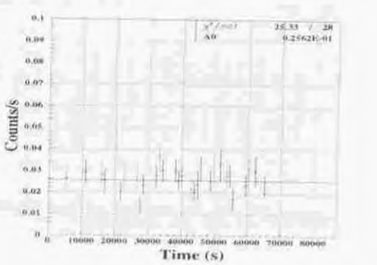

N1365 SW-source SIS

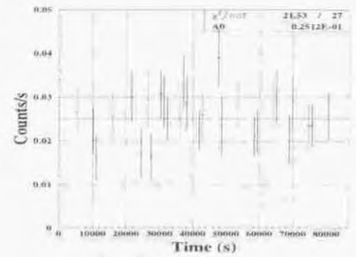

N2403 S3 SIS

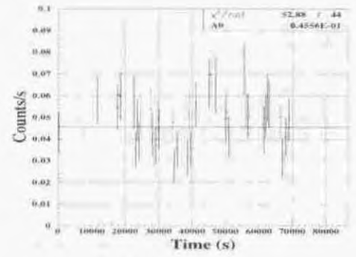

N2403 S3 GIS

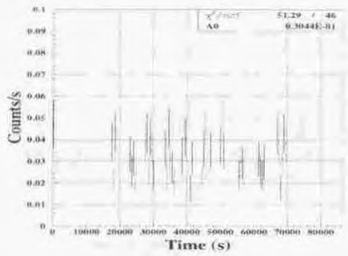

N3628 off-center GIS

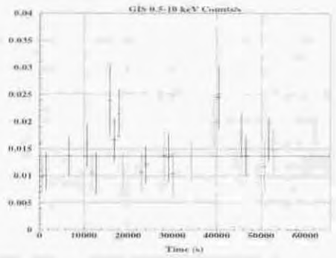

N4565 SIS

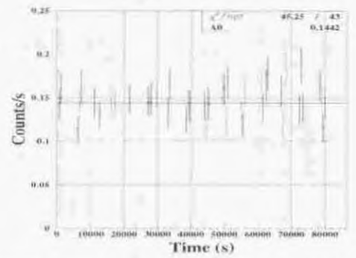

N4565 GIS

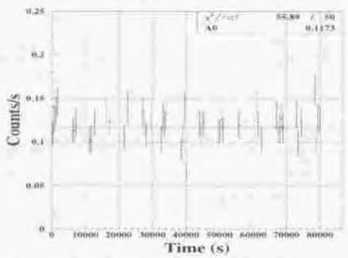

SNR in N6946 94/12 SIS

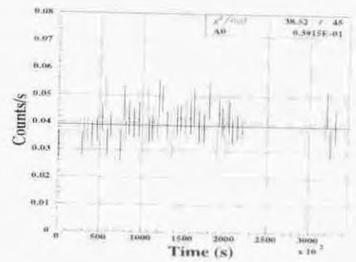

IC 342 S1 SIS

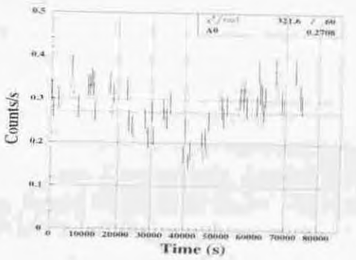

IC 342 S1 GIS

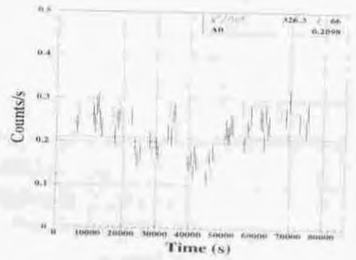

IC 342 S2 SIS

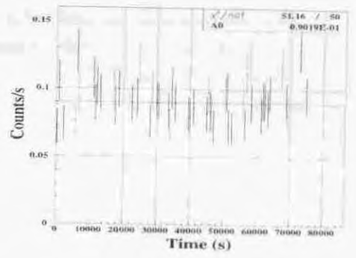

IC 342 S2 GIS

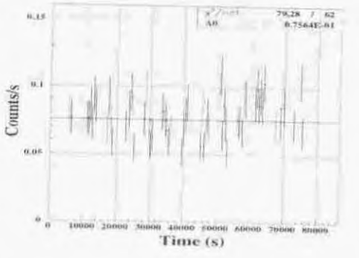

Dwingeloo 1 X-1 SIS

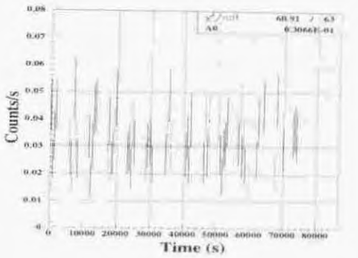

Dwingeloo 1 X-1 GIS

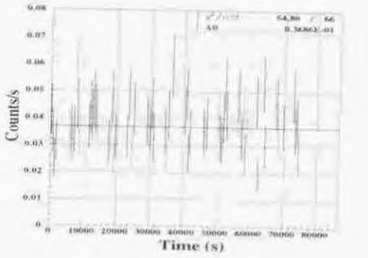

Acknowledgement

First of all, I would like to express my best gratitude to my supervisor Prof. K. Makishima for his support and guidance for this thesis. He has also led me throughout five years of my graduate course, taught me a lot in physics, astronomy, and others. I would also greatly thank to Prof. T. Kamae, for a lot of leading and encouragement. In addition, I should give my thanks to Dr. M. Tashiro and Dr. Y. Fukazawa for their continuous support and guidance in many aspect during my school life. I am also grateful to Ms. A. Kubota for various comments and discussions, which improve this thesis.

The *ASCA* observatory was developed, launched, and operated by *ASCA* team, including people at Institute of Space and Astronautical Science (ISAS), University of Tokyo, Tokyo Metropolitan University, Institute of Physical and Chemical Reserch (RIKEN), National Space Development Agency of Japan (NASDA), Nagoya University, Osaka University, Kyoto University, Iwate University, and Miyazaki University. I would like acknowledge to all the members of the *ASCA* team for their great efforts. Especially I wish to express my appreciation to the members, past and present, of the cosmic X-ray astronomy group in the University of Tokyo, including Dr. Y. Ishisaki, Dr. H. Kaneda, Dr. K. Matsushita, Dr. H. Kubo, Dr. Y. Saito, Dr. T. Tamura, Dr. H. Ezawa, Dr. K. Matsuzaki, Ms. E. Idesawa, Dr. N. Iyomoto, Mr. T. Otsuka, Mr. N. Tsuchida, Mr. H. Obayashi, Mr. G. Kawaguchi, Ms. A. Kubota, Mr. K. Nakazawa, Mr. M. Kokubun, Ms. S. Onone, Mr. N. Isobe, Ms. Y. Matsumoto, Mr. Y. Terada, Mr. T. Onishi, Mr. M. Sugiho, Mr. Y. Ezoe, Mr. J. Kotoku, and Mr. I. Takahashi. I am also grateful to Mr. J. Kataoka, Mr. T. Miyazaki, and Mr. H. Ozawa, among many people in other institutes.

Finally, I don't know how to express my thanks to my family for their warm support and understanding.